RSC Advances

PAPER

View Article Online
View Journal | View Issue



Cite this: *RSC Adv.*, 2025, **15**, 42910

# Ternary nanocomposite ReMIL-CN ($ReSe_2$@MIL-53(Fe)@g-$C_3N_4$) for energy storage and electroactive integrated $H_2O_2$ sensor application

Sohail Mumtaz,[a] Sameerah I. Al-Saeedi,[b] Saba Khalil,*[c] Abhinav Kumar,*[de] Amir Muhammad Afzal,[a] M. A. Diab*[fg] and Heba A. El-Sabban*[hi]

Integrated electrochemical systems capable of simultaneous charge storage and biochemical sensing response have gained prominence in modern materials science and biomedical engineering by offering multifunctionality for next-generation smart devices. The present comprehensive study is focused on the synthesis and characterization of a ternary nanocomposite material, focusing on its applications in integrated electrode systems for BHSCs and hydrogen peroxide ($H_2O_2$) sensing. The synthesized ReMIL-CN ($ReSe_2$@MIL-53(Fe)@g-$C_3N_4$) nanocomposite exhibits an average crystallite size of 27.27 nm, a specific surface area of 154 $m^2\ g^{-1}$, and a specific pore volume of 0.022 $cm^3\ g^{-1}$. The ReMIL-CN electrode offers maximum specific capacities ($Q_s$) of 1925.5 C $g^{-1}$ in a three-electrode testing setup and 423 C $g^{-1}$ in a ReMIL-CN//AC full-cell setup. The values of the oxidation and reduction diffusion coefficients ($D_{oxidation}$ and $D_{reduction}$) of the ReMIL-CN compound are 4.59 × $10^{-8}$ $m^2\ s^{-1}$ and 1.45 × $10^{-8}$ $m^2\ s^{-1}$, respectively. The highest obtained values of the energy density ($E_d$) and power density ($P_d$) are 50 Wh $kg^{-1}$ and 2060 W $kg^{-1}$, respectively. The ReMIL-CN//AC hybrid device demonstrates high stability response, with 95% capacity retention, 90% columbic efficiency, and 90% and 84% charge–discharge time retention over a prolonged period of 10 000 repeated cycles. The measured *b*-values of 0.59, 0.68, and 0.70 suggest the hybrid-natured operational mechanism of the ReMIL-CN//AC device. Moreover, the present composite-based electrode exhibits a sensitivity of $S$ = 0.185 μA $\mu M^{-1}$ $cm^2$ with a linear operational range of 50–1000 μM for the $H_2O_2$ detection system. The device maintains 95% signal stability after 1000 cycles, with an LOD of 0.1 μM, a linear regression value of $R^2$ = 0.998, and a minimal response time of less than 3 seconds, demonstrating the excellent selectivity of the device. The outstanding electrochemical charge storage and sensing capabilities of this ternary nanomaterial enable its integration into real-time, self-powered bioelectrochemical monitoring for next-generation portable and wearable bioelectronics.

Received 1st September 2025
Accepted 20th October 2025

DOI: 10.1039/d5ra06541k

rsc.li/rsc-advances



[a]*Department of Chemical and Biological Engineering, Gachon University, 1342 Seongnamdaero, Sujeong-gu, Seongnam-si 13120, Republic of Korea*

[b]*Department of Chemistry, College of Science, Princess Nourah bint Abdulrahman University, P. O. Box 84428, Riyadh 11671, Saudi Arabia*

[c]*Department of Physics, Riphah International University, Campus Lahore, Lahore, Pakistan. E-mail: sabakhalil537@gmail.com*

[d]*Centre for Research Impact & Outcome, Chitkara University Institute of Engineering and Technology, Chitkara University, Rajpura, 140401, Punjab, India. E-mail: drabhinav.urfu@gmail.com*

[e]*Department of Mechanical Engineering and Renewable Energy, Technical Engineering College, The Islamic University, Najaf, Iraq*

[f]*Department of Biotechnology, Yeungnam University, Gyeongsan, Gyeongbuk 38541, South Korea. E-mail: mohamed.a.diab@yu.ac.kr*

[g]*Water Analysis Department, Central Public Health Laboratories, Ministry of Health and Population, Cairo 11613, Egypt*

[h]*Integrated Materials Chemistry Laboratory, School of Materials Science and Engineering, Yeungnam University, Gyeongsan 38541, Republic of Korea. E-mail: heba_elsabban@yu.ac.kr*

[i]*Analysis and Evaluation Department, Egyptian Petroleum Research Institute (EPRI), 1 Ahmed El Zomor St. Nasr City, Cairo 11727, Egypt*

## 1 Introduction

Efficient electrochemical energy storage and conversion technologies are pivotal for addressing the rising global energy requirements and environmental issues.[1–4] The foremost challenge in this field is the development of high-energy- and high-power-density delivery systems with long-term operational periods.[5–7] Supercapacitors (SCs) and batteries are widely accepted as safe, clean, and green electrochemical entities for power sector applications.[8–11] However, batteries inherently suffer from slower charge–discharge rates, while supercapacitors have comparatively lower energy storage capacities. The synergistic integration of these two devices into a single hybrid system helps overcome their limitations.[12,13] Such hybrid systems can facilitate both rapid energy release and high energy retention along with efficient lifespans and cost-effectiveness, making these battery-hybrid supercapacitors (BHSCs) highly suitable for efficient energy storage systems.[14–17] Integrated

detection systems based on these electrochemical BHSC devices have also emerged as powerful analytical tools for food and water quality monitoring and medical diagnostics.[18–20] The capabilities of these BHSC devices for holding high energy density *via* a rapid charge–discharge process enable them to achieve efficient, real-time, and portable electrochemical sensing response. Such electrochemical systems can be used for contaminant detection in the food and water quality sectors to ensure public health safety and in medical field applications, where these hybrid systems enable sensitive, selective, and trace-level detection of different biomarkers and chemicals, along with efficient power storage and supply.[21–24] Hydrogen peroxide ($H_2O_2$) is a commonly used chemical in household, medical, and industrial applications. However, it can also cause severe health risks depending on its concentration and exposure method. Therefore, early and trace-level detection and proper handling of $H_2O_2$ are essential to minimize these risks.[25,26]

The pursuit of enhanced performance in hybrid energy devices has directed researchers towards the development of advanced electrode materials.[27–29] A variety of composite materials combining metallic, organic, and inorganic components, such as MOFs, TMDs, TMOs, TMSs, HKUSTs, conductive polymers, and MILs, have drawn significant attention owing to their unique structural features, high surface areas, and tunable porosities, which make them ideal for dynamic charge storage applications.[30,31] These materials enhance charge accommodation and transport, increase the specific energy and power density, and improve the charge–discharge capabilities, leading to high energy storage and rapid pulsation response applications.[32–34] The advancements in electrode materials have also enhanced the sensitivity, selectivity, and stability of these electrode-based sensors.[35] Integrating detection systems with hybrid energy storage mechanisms improves operational longevity and supports self-powered sensing applications, leading to multifunctional electrochemical sensing systems for remote and point-of-care diagnostics.[36,37]

Subhani, Karamat, *et al.* stated that the $MnO_2$-decorated carbon fiber has the highest specific capacitance of 1.71 F $g^{-1}$ and an energy density of 3.8 Wh $kg^{-1}$ with a 123.6 MPa mechanical strength in supercapacitor-illuminated LEDs.[38] Xia, Changlei, *et al.* reported a $CoFe_2O_4$/GNRs electrode offering specific capacitances of 922 F $g^{-1}$ and 487.85 F $g^{-1}$ in an asymmetric supercapacitor cell system, with the highest power and energy densities of 6730.76 W $kg^{-1}$ and 32.8 Wh $kg^{-1}$, respectively.[39] Zhang, Fan, *et al.* presented a staged intercalation–deintercalation mechanism in the $LiFePO_4$-hybrid-graphite electrode, with an energy density of 176.7 Wh $kg^{-1}$, good capacity, and efficient stability for over 3500 consecutive repeated cycles.[40] Hu, Pu, *et al.* presented a novel sodium-based $NaV_3(PO_4)_3$/C electrode for battery testing, exhibiting a capacity of 146 mAh $g^{-1}$ in a Na half-cell study and 80% capacity retention after 1000 cycles in a symmetric electrode full-cell configuration.[41] Sakthivel, P., *et al.* reported the development of a $MoS_2$-$Bi_2S_3$@CNT-alkaline electrolytic system having a specific capacitance of 1338 F $g^{-1}$, a 99.5% stable columbic efficiency response over 10 000 cycles, and 60% and 34.6% retention stability responses over 2000 and 10 000 cycles, respectively.[42] Cui, Xiaosha, *et al.* reported aqueous $MnO_2$ electrode-based AEESD energy devices exhibiting a high energy density of 0.12 mWh $cm^{-2}$ and a long lifespan, with a capacitance of 1551 mF $cm^{-2}$, and 89.63% stable capacitance retention.[43] Sahoo, Ramkrishna, *et al.* reported a highly stable rGO@$VO_2$ heterostructured anode-based BSH with AC@CC as the cathode, which exhibited the specific capacity, energy, and power of 1214 mAh $g^{-1}$, 126.7 Wh $kg^{-1}$, and 10 000 W $kg^{-1}$, respectively.[44] Alam, Faiz, *et al.* reported the $Co_3(PO_4)_2$@PANI hybrid system possessing a power density of 6027 W $kg^{-1}$, a 97.6% cyclic stability, an 87% columbic efficiency, and an energy density of 7.1 Wh $kg^{-1}$ in a supercapattery-type assembly.[45] Nguyen, P. *et al.* reported $TiO_2$/$TiS_2$ for lithium–sulfur batteries with an energy density of 331 Wh $kg^{-1}$ and good cyclic response.[46] Ahmad, Awais, *et al.* reported aqueous hybrid supercapacitors (AHSCs) using CCO ($CoCr_2O_4$) electrodes, exhibiting a specific capacitance of 2951 F $g^{-1}$, a minimum charge transfer resistance ($R_{ct}$) value of 0.135 Ω, and 98.7% stable capacitance retention response.[47] He, Jiarui, *et al.* reported Na–S batteries having an energy density of 1274 Wh $kg^{-1}$ and a discharge capacity of 1081 mAh $g^{-1}$.[48] Zhang, Fan, *et al.* reported a graphene-enhanced $Fe_3O_4$ electrode with a 3D graphene electrode in a supercapacitor-battery hybrid system, which had the highest energy and power density values of 147 Wh $kg^{-1}$ and 2587 W $kg^{-1}$, respectively.[49] Zhang, Yang, *et al.* reported a lithium-ion capacitor-based system comprising AC negative and graphite positive electrodes, which exhibited the highest energy and power densities of 200 Wh $kg^{-1}$ and 7.7 kW $kg^{-1}$, respectively.[50] Naresh, Nibagani, *et al.* presented advanced AZIBs based on an α-$MnO_2$@$SnO_2$ nanocomposite, which exhibited the highest capacity value of 347 mAh $g^{-1}$.[51] Polat, Bulent, *et al.* reported the ZnO@polypyrrole-P(VSANa) electrode for $H_2O_2$ detection and a symmetric SC configuration, with a 0.044 μM LOD value and a 171.8 F $g^{-1}$ specific capacitance value.[52] Zhao, Jingyuan, *et al.* reported the monometallic elemental $Ti_3C_2T_x$-MXene ($Mo_2TiC_2T_x$) demonstrating a capacitance of 398 F $cm^{-3}$ with 82.75% capacitance maintenance and volumetric energy and power densities of 48.1 W h $L^{-1}$ and 230.7 W $L^{-1}$, respectively.[53] Xiong, Chuanyin, *et al.* proposed 3D bifunctional CMT@N-rGO carbon microtubes hybridized with $MnO_2$ and PANI, having good supercapacitive and ORR response, presenting excellent rate performance during charge/discharge, 95% and 93% capacitance retention, and high energy efficiencies of 65–77% and 61–72% for both CMT@N-rGO@$MnO_2$ and CMT@N-rGO@PANI electrodes, respectively.[54] Mohammad, Akbar, *et al.* reported a CC-modified $Al_2O_3$-g-$C_3N_4$ nonenzymatic electrochemical sensor for $H_2O_2$ detection having an LOD value of $1.6 \times 10^{-4}$ M and a sensitivity of 108 μA $mM^{-1}$ $cm^{-2}$.[55]

Continuing the usage of conventional transition-metal-based materials, the present study explores rhenium (Re) and its selenide derivatives as promising base materials owing to their distinctive 5d electronic configurations and multivalent oxidation states of $Re^{4+}$ and $Re^{6+}$. Unlike traditional 3d transition metals, Re possesses a broader d-band dispersion and a stronger spin–orbit coupling, which will promote rapid charge

transfer and enhance the intrinsic electrical conductivity of the electrode. Moreover, rhenium diselenide ($ReSe_2$) exhibits a distorted 1T lattice with abundant active edge sites and anisotropic in-plane electrical pathways, offering a unique advantage for facilitating multielectron redox reactions and improving the catalytic conversion of electroactive species. To further optimize electronic and ionic transport kinetics, the MIL-53 (Fe-MOF) host is selected as a structural backbone. It offers a high surface area, an adjustable pore architecture, and metal–ligand coordination-driven design flexibility. The porous MOF matrix provides uniform anchoring sites for $ReSe_2$ nanostructures, suppressing particle aggregation while establishing well-defined channels for electrolyte infiltration and charge migration. Such synergistic integration of $ReSe_2$ within the MOF is anticipated to yield a composite with enhanced structural integrity, accessible reaction interfaces, and accelerated redox kinetics during electrochemical operation. Along with this, we have incorporated graphitic carbon nitride (g-$C_3N_4$) as a dopant. This heteroatom dopant is introduced to modulate the electronic structure and generate interfacial defects that facilitate charge delocalization between the $ReSe_2$ and the MOF matrix. The dopant g-$C_3N_4$ atoms act as electron donors, enriching the local charge density and creating polar sites due to their intrinsic physicochemical properties. This plays a significant role in enhancing the electrochemical response to improve the adsorption and catalytic transformation of electroactive intermediates. The 2D graphitic-like structure of g-$C_3N_4$ provides a high surface area, abundant active sites, and a π-conjugated network that promotes efficient electron transport. The nitrogen-rich framework of g-$C_3N_4$ offers multiple lone-pair electrons, facilitating strong coordination and charge transfer interactions with transition metal species such as Re and Fe within $ReSe_2$ and MIL-53, respectively. This leads to accelerated redox kinetics and improved electrical conductivity across the hybrid interface. g-$C_3N_4$ also serves as a structural buffer and a conductive matrix, preventing the agglomeration of $ReSe_2$ nanosheets and MIL-53 particles while maintaining mechanical integrity during repeated charge–discharge cycles. This novel, tailored, and electronically modulated ReMIL-CN composite material is expected to establish a rational framework for developing a multifunctional electrode architecture that unites high electrical conductivity, abundant active sites, and robust structural stability, ultimately advancing the performance of electrochemical energy storage and conversion devices.[56]

In this work, we aimed to elucidate the mechanism and performance of supercapatteries (BHSCs) and $H_2O_2$ sensors by investigating the structure and morphology of the synthesized ReMIL-CN nanocomposite material and its electrochemical performance.

## 2 Experimentation

### 2.1 Materials and methods

The following analytical-grade reagents and chemicals were used in the synthesis process of the composite materials. The rhenium (Re) and selenium (Se) powder precursors were sourced from Sigma-Aldrich; terephthalic acid, KOH, and activated carbon (AC) were bought from Molychem; and iron(III) nitrate nonahydrate ($Fe(NO_3)_3\cdot 9H_2O$) was obtained from Alfa Aesar. Hydrazine hydrate ($N_2H_4\cdot H_2O$), *N*,*N*-dimethylformamide, urea ($CO(NH_2)_2$), ethanol, and DI water were utilized as solvents.

The ReMIL-CN composite material was synthesized *via* a sequential hydrothermal and solvothermal approach. g-$C_3N_4$ was synthesized *via* the green hydrothermal method using the low-cost, ecofriendly nitrogen-rich urea precursor. For this, a 1 M precursor solution of urea in DI water was prepared by dissolving and stirring to ensure complete dissolution and homogeneity. By heating in the autoclave at 170 °C for 8 hours, the polymerized g-$C_3N_4$ was formed. The g-$C_3N_4$ product was precipitated after cooling, washed, dried, ground, and preserved for use.

To synthesize $ReSe_2$, a stoichiometric mixture of Re and Se powders was mixed in a 1 : 2 molar ratio and dispersed in 40 mL of deionized water under vigorous magnetic stirring. A small amount of hydrazine hydrate ($N_2H_4\cdot H_2O$) was added as a reducing agent, which enhanced the solubility of materials and facilitated the reaction kinetics. The resulting suspension was autoclaved at 190 °C for 12 hours. The resultant $ReSe_2$ precipitated product was naturally cooled, washed several times to remove unreacted materials, and dried in a vacuum oven at 60 °C for 12 hours.

For MIL-53 (Fe-MOF) synthesis, a 50 mL 1 M solution containing $Fe(NO_3)_3\cdot 9H_2O$, terephthalic acid ($C_8H_6O_4$), DMF, and DI water was prepared. $Fe(NO_3)_3\cdot 9H_2O$ was the metal source, and terephthalic acid ($C_8H_6O_4$) was the organic linker. It was subjected to continuous stirring to form a homogeneous solution. The prepared solution was poured into a 50 mL Teflon-lined stainless-steel autoclave, sealed tightly, and subjected to a hydrothermal process under heating at 150 °C for 12 hours. After natural cooling to room temperature, the resulting reddish-brown precipitate was collected by centrifugation. It was then thoroughly washed to remove unreacted precursors and residual solvents and dried in a vacuum oven at 60 °C for 12 hours.

To synthesize the $ReSe_2$@MIL-53@g-$C_3N_4$ hybrid composite, equimolar aqueous dispersions of the presynthesized $ReSe_2$, Fe-based MIL-53, and g-$C_3N_4$ were prepared. These components were then mixed in a 2 : 1 : 1 ratio under continuous magnetic stirring for 30 minutes, ensuring uniform dispersion and effective interaction among all constituents. The resulting homogeneous suspension was subsequently transferred to a Teflon-lined stainless-steel autoclave and subjected to hydrothermal treatment at 180 °C for 12 hours, which facilitated the intimate interfacial coupling of $ReSe_2$ with MIL-53 and g-$C_3N_4$, leading to the formation of a well-integrated ternary ReMIL-CN composite structure. The resultant product was processed through subsequent steps into a finely ground powder for further use.

Fig. 1 comprehensively describes the novel synergistic integration in the ternary composite material. It highlights the structural morphologies involved, synthesis steps, and resulting hybrid structure that is supposed and justified to own the unique combined characteristics of all constituent materials. The

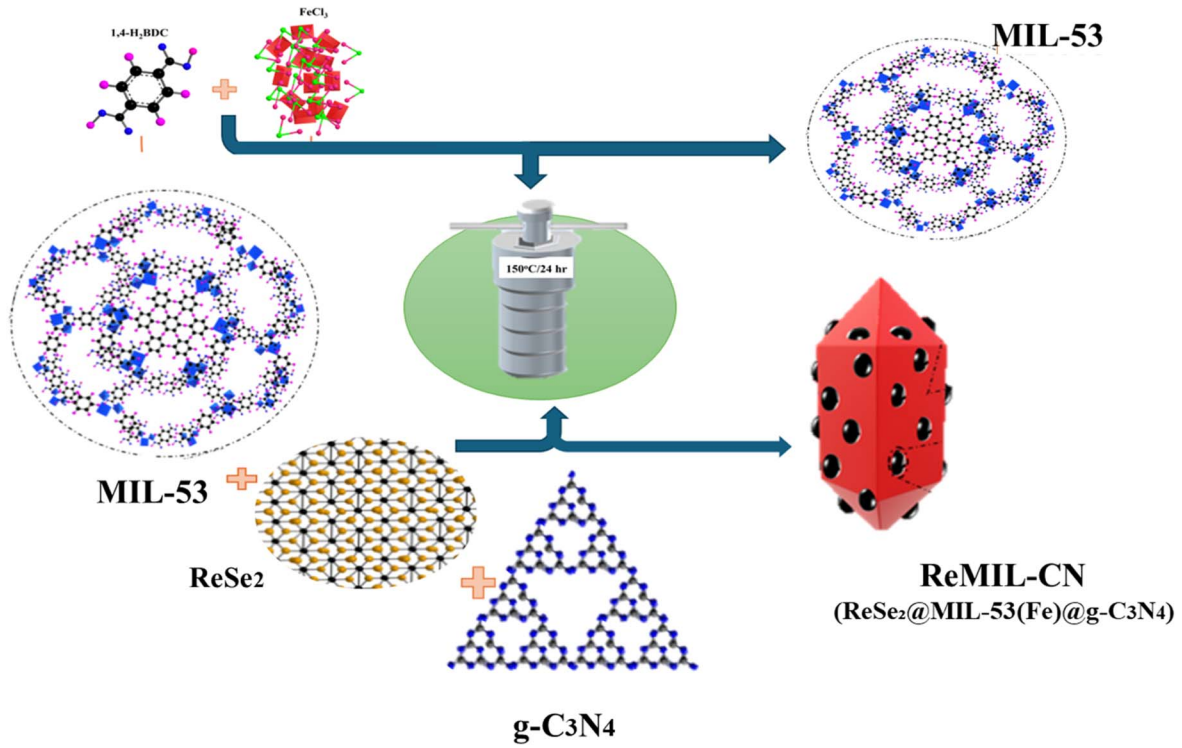


Fig. 1 Schematic showing the integration of $ReSe_2$, iron-MOF (MIL-53), and g-$C_3N_4$ into the hybrid ternary composite material ReMIL-CN.

resultant composite material is represented by a red octahedron with an embedded Fe-MOF (framework) and $ReSe_2$ nanoparticles. The structural components, including the porous Fe-MOF and the $ReSe_2$ layer, are also exhibited in Fig. 1.

The morphology and surface texture of the synthesized materials were examined using scanning electron microscopy (SEM) (JEOL JSM-6510LV) operated at an accelerating voltage of 10–15 kV. SEM energy-dispersive X-ray spectroscopy (EDX) was employed to determine the elemental composition and distribution, confirming the successful incorporation of the constituent elements. The crystalline structure of the samples was analyzed by X-ray diffraction (XRD) using a Cu-K$\alpha$ radiation source with a wavelength of $\lambda = 1.5406$ Å, operating at 40 kV and 30 mA. The obtained diffraction peaks were matched with the standard JCPDS data to identify the corresponding crystalline phases. The specific surface area and pore size distribution were determined from $N_2$ adsorption–desorption isotherms using a BET analyzer (Micromeritics ASAP 2460). The Brunauer–Emmett–Teller (BET) method was applied to calculate the surface area, while the Barrett–Joyner–Halenda (BJH) model was used to determine pore size and pore volume.

Electrochemical measurements were carried out using a standard three-electrode system connected to an electrochemical workstation (Corrtest). During electrochemical characterization, the prepared electrode served as the working electrode, a platinum wire as the counter electrode, and Hg/HgO as the reference electrode. All measurements were conducted in a 1 M KOH aqueous electrolyte solution at room temperature. Cyclic voltammetry (CV), galvanostatic charge–discharge (GCD), electrochemical impedance spectroscopy (EIS), and Dunn's model tests were performed to evaluate the redox behavior, charge storage mechanism, specific capacity, cyclic stability, internal resistance and charge transfer dynamics, and energy and power densities.

After the parametric study of the fabricated electrodes, the study was extended to a real BHSC hybrid device and an electrochemical $H_2O_2$ sensing system. In the BHSC device, the active material positive electrode and activated carbon (AC) negative electrode were asymmetrically configured. The mass balance between the positive and negative electrodes was optimized according to the following charge balance relation to ensure the stable and efficient charge storage performance of the device:

$$m^+C^+V^+ = M^-C^-V^- \quad (1)$$

For $H_2O_2$ sensing evaluation, the three-electrode electrochemical setup was employed, comprising the active material-based modified electrode as the WE, a platinum (Pt) wire as the CE, and Hg/HgO as the RHE.

### 2.2 XRD and scanning electron microscopy (SEM)

The obtained XRD pattern confirmed the successful incorporation of all three components without impurity phases. The diffraction pattern in Fig. 2(a) reveals the distinct reflections for individual components g-$C_3N_4$, MIL-53(Fe), and $ReSe_2$ and the hybrid ternary compound. The obtained XRD peaks corresponding to each constituent, without any significant impurity signals, confirmed the successful synthesis of the ternary hybrid ReMIL-CN composite material. For g-$C_3N_4$, the characteristic

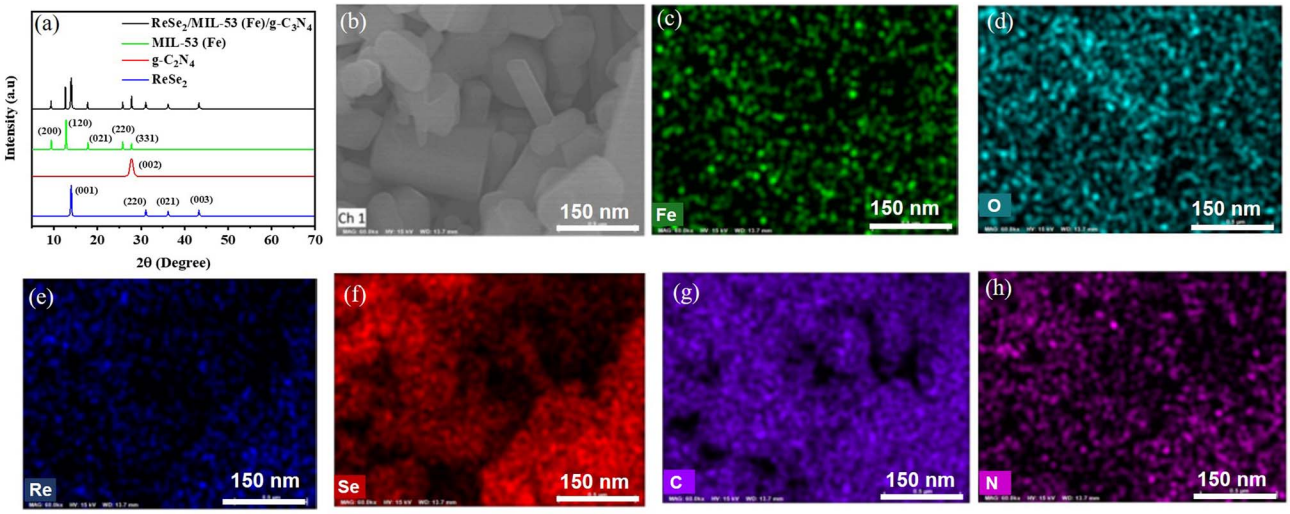


Fig. 2 (a) XRD characterization, (b) SEM image, and (c–h) SEM-EDX analysis.

peaks were observed at $2\theta = 12.8°$ and 27.6°, analogous to the (100) and (002) *hkl* planes, respectively. These indexed peaks are the characteristic fingerprints of g-$C_3N_4$, indicating the in-plane tri-*s*-triazine repeated structural units and interlayer stacked conjugated aromatic planes. This corresponds to the periodic arrangement and structural repetition within the 2D layers of g-$C_3N_4$ (JCPDS no. 87-1526).[57] MIL-53(Fe) exhibited characteristic sharp peaks at $2\theta = 9.2°$, 12.0°, 17.1°, 18.5°, and 25.6°, indexed to the (200), (120), (220), (021), and (331) planes, respectively. The obtained peaks at $2\theta$ values of 9.2°, 12.6°, and 17.6° corresponded to the hydrated crystalline form of MIL-53(Fe) and match well with the previously reported results for Fe-based MOFs. For $ReSe_2$, the sharp reflections found at $2\theta$ values of 13.6°, 31.2°, 38.7°, and 44.0° corresponded to the (001), (220), (021), and (003) planes, respectively, confirming the triclinic phase structure of $ReSe_2$ with a dominant growth orientation along the (00l) plane (*c*-axis alignment). These peak intensities and positions matched well with JCPDS file no. 04-007-1113.[58] The obtained XRD pattern of the present ReMIL-CN composite material demonstrated a combined diffraction pattern that retained all major reflections from its constituent materials. The sharpness of the peaks for the hybrid composite also confirmed the purity and ordered atomic arrangement within the structure. These findings confirmed the successful synthesis of the well-crystalline ReMIL-CN hybrid nanocomposite with the synergistic structural integration of $ReSe_2$, MIL-53(Fe), and g-$C_3N_4$.

The XRD results were used to ascertain the degree of crystallinity, lattice parameter, phase angle, and phase composition of the presented ReMIL-CN nanocomposites. The average crystallite size ($D$) of the composite was measured from the intensity and width of these peaks using the Debye–Scherrer equation:

$$D = \frac{K\lambda}{\beta \cos \theta} \quad (2)$$

Here, "$D$" represents the crystallite size, "$K$" is the Scherrer constant (typically 0.9), "$\lambda$" denotes the X-ray wavelength (1.5406 Å), "$\beta$" is the full width at half-maximum (FWHM), expressed in radians, and "$\theta$" is the Bragg diffraction angle.

The synthesized ReMIL-CN composite material's average crystallite size was measured perpendicular to the (002) planes at $2\theta = 27.6°$, which was 27.27 nm, and the FWHM was 0.3°. This demonstrates the nano-sized dimensions of the stacked composite, corresponding to the vertical crystalline coherence length.

The SEM characteristic image of the presented ReMIL-CN nanocomposite, shown in Fig. 2(b), provided valuable insights into the morphological architecture and structural integrity of the synthesized nanocomposite. It displayed a highly porous, flake-like morphology with densely packed interconnected nanosheets and agglomerated irregular-shaped particulates, forming a hierarchical structure. The nano-scale features with dimensions well below 150 nm confirmed the formation of a nanostructured hybrid composite. The sheet-like layered structure in the SEM image indicated the presence of exfoliated g-$C_3N_4$ layers in the composite. These nanosheets appeared to be thin and crumpled, providing a large surface area and abundant edge sites for electrochemical interactions. The irregularly embedded granular particles within these layers were likely due to the MIL-53(Fe) and $ReSe_2$ constituents. The granular features suggested that the MIL-53(Fe) MOF had been successfully incorporated into the composite and retained its porous structure within the hybrid matrix. The existence of flake like structure is typically exhibited by the $ReSe_2$ and integrated into the porous framework, forming strong interfacial contact with the g-$C_3N_4$ nanosheets and the MOF matrix. The uniform and loosely stacked layered structure indicated the mesoporous nature of the presented synthesized hybrid ternary composite, leading to enhanced ion diffusion and an enhanced available surface area for electrochemical reactions. The mesoporous architecture of the present composite, without isolated and

large particles, as shown in the SEM image, suggested good compatibility among its components and the successful hybridization of the material. This well-integrated structure indicated the potential robustness and stability of the composite material during practical applications, including biosensing, photocatalysis, and supercapacitor electrodes.

The images in Fig. 2(c–h) display the results of SEM-EDX spectroscopy, providing the qualitative elemental mapping of the presented synthesized hybrid composite material. This energy-dispersive X-ray coupled SEM analysis provided the detailed spatial distribution and relative abundance of the constituent elements across the sample. The EDX elemental mapping confirmed the successful incorporation and even dispersion of the constituent elements across the composite's surface, demonstrating the successful synthesis and potential synergy among components. The uniform distribution of iron (Fe) in Fig. 2(c) and rhenium (Re) in Fig. 2(d) confirmed their successful codeposition within the material matrix. The widespread and dense distribution of selenium (Se) is shown in Fig. 2(d), indicating its potential role as a major active site-contributing component of the material. The uniformly dispersed carbon (C) and oxygen (O) typically originated from the carbon-based (g-$C_3N_4$) support structure and possible surface oxidation. Elemental nitrogen (N), as shown in Fig. 2(h), was less densely distributed but was still present across the sample, indicating potential N doping, which can enhance the conductivity and surface reactivity of the composite material. This elemental homogeneity demonstrated the consistent composition of the synthesized material, making it critical for achieving reliable responses in electrocatalysis-based sensors and energy storage devices.

### 2.3 Electrochemical studies: CV, GCD, and EIS

The electrochemical performance of the fabricated electrodes was systematically evaluated by cyclic voltammetry (CV) and galvanostatic charge–discharge (GCD) analyses. A 1 M KOH-DI water electrolyte solution was used for electrochemical measurements because of its efficient ionic conductivity, good charge transfer ability, and efficient operational suitability with transition metal-based materials.

The CV plots shown in Fig. 3(a–c) display the current response of the $ReSe_2$, MIL-53(Fe)@$ReSe_2$, and hybrid compound electrodes at varying scanning potentials from 3 mV $s^{-1}$ to 50 mV $s^{-1}$ *versus* RHE. Each electrode exhibited well-defined redox peaks, corresponding to the occurrence of redox reactions within these electrode materials. The pronounced Faradaic characteristic peaks obtained in CV plots reflected the battery-like behavior of these electrodes. Among the results of the three samples, the ternary composite ReMIL-CN electrode demonstrated more pronounced and symmetric redox peaks,

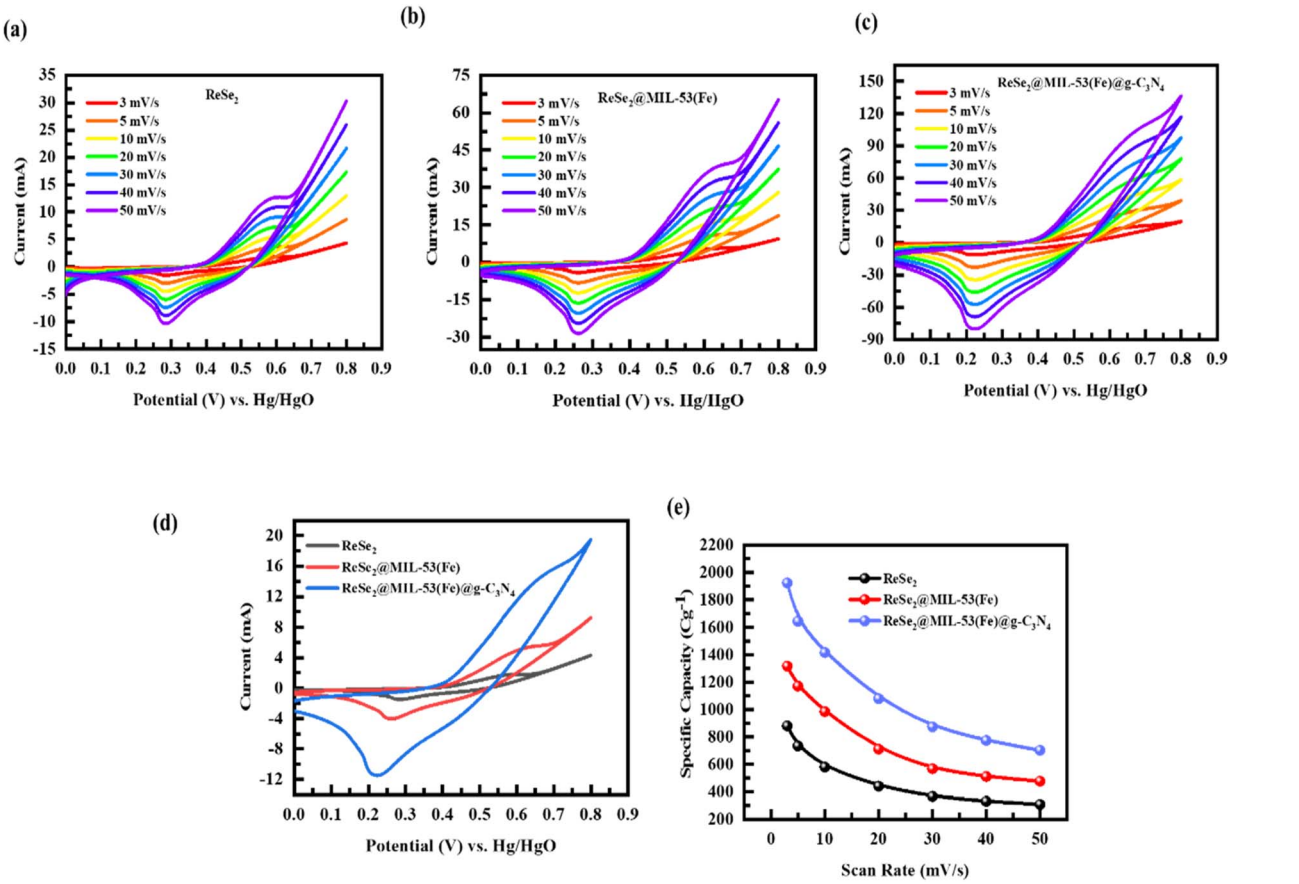


Fig. 3 CV curves of (a) $ReSe_2$, (b) MIL-53(Fe)@$ReSe_2$, and (c) the ReMIL-CN composite for the scan rate range of 3-50 mV $s^{-1}$, (d) comparative CV performance of the three electrodes at 50 mV $s^{-1}$, and (e) specific capacity *versus* scan rate for the three electrodes, calculated from CV results.

indicating the enhanced electrochemical reversibility and redox kinetics of this electrode. These peaks originated from the synergistic redox transitions of iron ($Fe^{3+}/Fe^{2+}$) in the MIL-53(Fe) framework and $Re^{4+}/Re^{3+}$ in $ReSe_2$, accompanied by reversible ion intercalation/deintercalation processes within the hybrid matrix.[59] The strong current response and nearly symmetric redox peaks indicated high reversibility and fast ion diffusion kinetics. This suggested that both surface and bulk faradaic reactions actively contributed to charge storage. The symmetric CV curves indicated balanced charge/discharge cyclic processes and minimal internal resistance, leading to a high electrochemical charge storage response obtained for the presented synthesized novel composite-based electrode, with stable charge storage mechanisms and durability during repeated cycles. The rise in the current with an increase in the voltage demonstrated an enhanced charge storage capacity and conductivity at high voltage values. The narrow gaps between forward and reverse branches demonstrated a minimal overpotential, ensuring efficient energy conversion in the electrode-based system. Based on the comparison of the CV curves of three composite materials' electrodes, the ReMIL-CN composite electrode showed a more pronounced faradaic mechanism, especially under higher input conditions, making it a promising candidate for energy storage applications.

The specific capacity ($Q_s$) *versus* scan rate values presented in Fig. 3(e) were measured from the CV characteristic results for the $ReSe_2$, MIL-53(Fe)@$ReSe_2$, and ReMIL-CN hybrid material electrodes using the following relation:

$$Q_s = \frac{1}{mv}\int_{vi}^{vf} I \times VdV \quad (3)$$

Here, $Q_s$ is the specific capacity (C $g^{-1}$), $m$ is the mass of the active material (g), $v$ is the scan rate (V $s^{-1}$), and $I$ is the current (A). The integration of the current over the potential range provided the total charge, which was normalized by the mass and scan rate, yielding $Q_s$. The values of the specific capacity decreased with increasing scan rate for all three electrodes due to limited ion diffusion at higher scan rates, which restricts the full utilization of active sites. Among the three tested materials, the hybrid composite material demonstrated the highest specific capacity consistently across all scan rates, reaching the highest value of 1925.5 C $g^{-1}$ at 5 mV $s^{-1}$ and maintaining the minimum value of 800 C $g^{-1}$ at 50 mV $s^{-1}$. Compared to the lower capacities achieved by MIL-53(Fe)@$ReSe_2$ and $ReSe_2$, the hybrid material electrode demonstrated a superior performance, likely due to the synergistic effects facilitated by the composite architecture of $ReSe_2$, Fe-MOF (MIL-53) and g-$C_3N_4$, suggesting that it is a favorable material for high-performance electrochemical energy storage systems. In addition to CV, GCD tests were also conducted for the $ReSe_2$-, MIL-53(Fe)@$ReSe_2^-$, and hybrid compound-based electrodes at varying current densities from 1 A $g^{-1}$ to 2.2 A $g^{-1}$, leading to a more direct assessment of the electrochemical performance of these electrodes. The GCD analysis illustrated in Fig. 4(a–c) provided

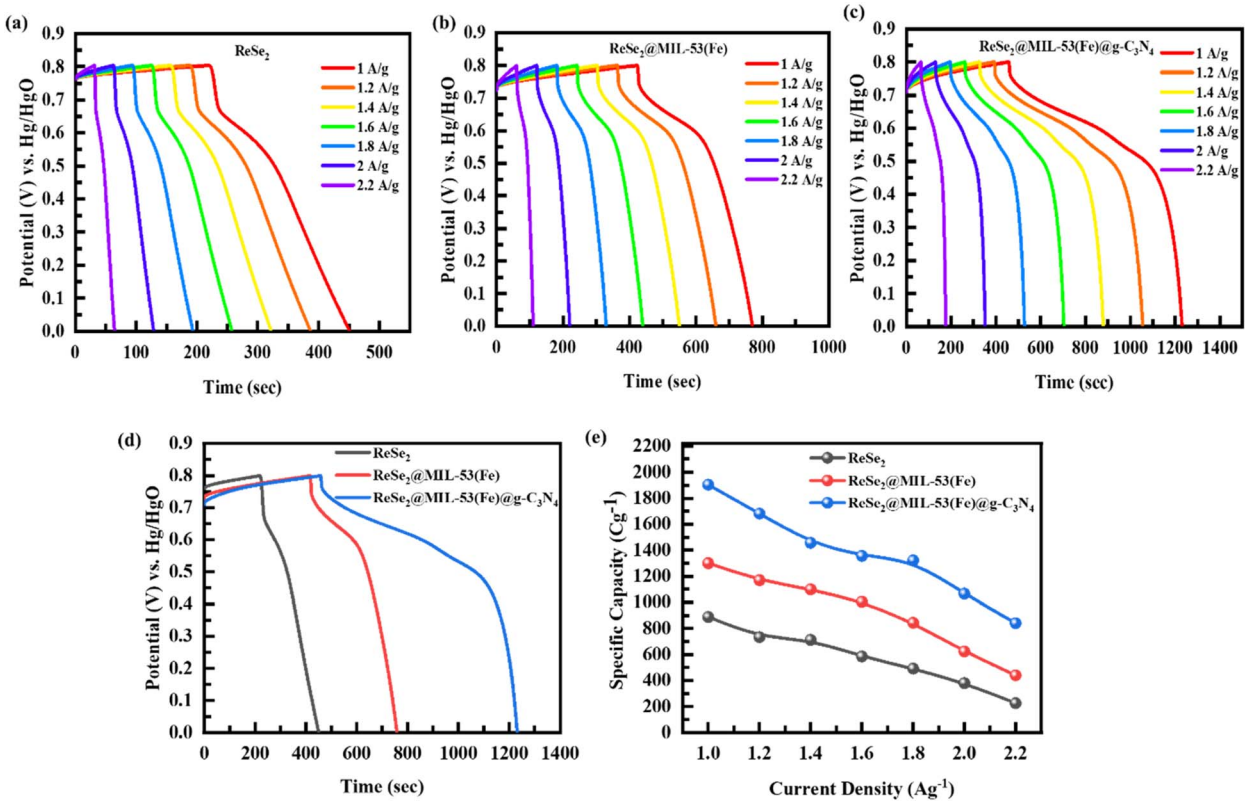


Fig. 4 GCD characteristics curves of (a) $ReSe_2$, (b) MIL-53(Fe)@$ReSe_2$, and (c) the ternary composite ReMIL-CN over the 1–2.2 A $g^{-1}$ input current range, (d) comparative GCD performance of the three nanocomposites at 50 mV $s^{-1}$, and (e) their measured specific capacity values.

symmetric charge–discharge profiles with distinct plateaus, further confirming the faradaic-dominated mechanism. The minimal potential difference between the charge and discharge plateaus for the ReMIL-CN electrode reflected the low polarization and excellent electrochemical kinetics of the hybrid electrode. The linear regions of GCD profiles demonstrated the good electrochemical activity and conductivity of the electrodes, and the relatively flat regions with linear slopes signified quick electron mobility throughout their devices. A gradual reduction in the discharge time of all three electrodes was observed as the current density increased, which is a typical behavior due to ion diffusion and kinetic limitations at higher current rates.

The GCD graphs suggested that the ReMIL-CN composite's electrode outperformed the individual components' electrodes. This electrode retained a relatively better capacity even at elevated current densities, suggesting the excellent rate capability and structural stability of this electrode-based system. The longest discharge times of this electrode indicated its highest specific capacity and superior electrochemical performance. It also corresponded to the stable ion storage response of the presented electrode-based device.

Fig. 4(d) presents the comparative GCD profiles of the three electrodes at 1 A $g^{-1}$, highlighting the performance superiority of the ReMIL-CN composite electrode over pristine $ReSe_2$ and MIL-53(Fe)@$ReSe_2$ electrodes. This enhanced performance arose from the synergistic combination within the composite electrode, making it a strong candidate for upgrading ionic accessibility, capacity, electrochemical stability, and discharge time stability for energy storage applications.

The electrochemical charge storage capability and rate performance of all three composite-based electrodes were assessed by calculating their specific capacity ($Q_s$) *versus* scan rate from their GCD results using the following equation:

$$Q_s = \frac{I \times \Delta t}{m} \quad (4)$$

Here, $I$ is the applied current, $\Delta t$ is the discharge time, and $m$ is the active mass of the material. The smooth and linear reduction in the specific capacity values with an increase in the current also showcased the material's capability to manage rapid ion movement without considerable capacity loss. The highest obtained values of the specific capacity were 1912 C $g^{-1}$ for the ReMIL-CN electrode, 1206.5 C $g^{-1}$ for MIL-53(Fe)@$ReSe_2$, and 858 C $g^{-1}$ for the $ReSe_2$ electrode. These measured specific capacities from CV and GCD were in proximity, and the slight variation (<1%) was attributed to differences in the charge–discharge kinetics and potential window integration during measurement. This close agreement confirmed the reliability of the electrochemical evaluation and highlighted the excellent charge storage ability of the ReMIL-CN composite's electrode.

The anodic and cathodic peak current *versus* square root of scan rate variations are depicted in Fig. 5(a–c) for the $ReSe_2$, MIL-53(Fe)@$ReSe_2$, and the ReMIL-CN sample materials, respectively, providing insights into their electrochemical performance. These plots also showed the linear relationship for the ion insertion and extraction processes. The plot in Fig. 5(a) for $ReSe_2$ exhibited its linear trends with relatively lower slopes. It indicated not only diffusion-controlled kinetics but also limited ion diffusion rates and conductivity, which constrained its charge storage capacity. The ReMIL-CN compound-based electrode resulted in a steeper concentration gradient due to its more pronounced CV peak currents and higher charge kinetic values for each input scan rate value.

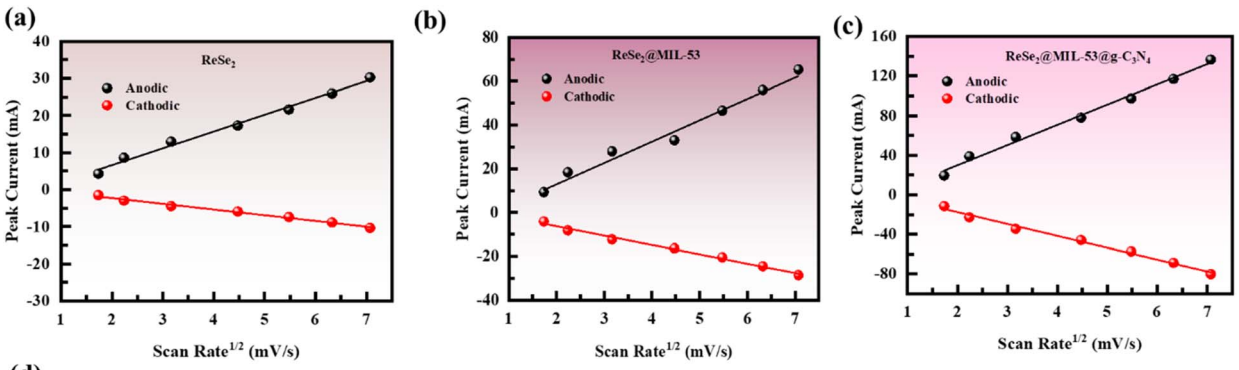


(d)

| Scan Rate mV/s | | 3 | 5 | 10 | 20 | 30 | 40 | 50 |
|---|---|---|---|---|---|---|---|---|
| ReSe2 | $D_{oxidation}$ | 4.87E-13 | 4.75E-13 | 4.87E-13 | 4.83E-13 | 4.75E-13 | 4.91E-13 | 4.87E-13 |
| ReSe2@MIL-53 | | 2.48E-12 | 2.54E-12 | 2.59E-12 | 2.54E-12 | 2.54E-12 | 2.50E-12 | 2.52E-12 |
| ReSe2@MIL-53@g-C3N4 | | 4.59E-08 | 4.61E-08 | 1.39E-11 | 1.40E-11 | 1.37E-11 | 1.37E-11 | 1.39E-11 |
| ReSe2 | $D_{reduction}$ | 5.67E-14 | 5.54E-14 | 5.68E-14 | 5.63E-14 | 5.54E-14 | 5.72E-14 | 5.67E-14 |
| ReSe2@MIL-53 | | 4.76E-13 | 4.87E-13 | 4.97E-13 | 4.87E-13 | 4.87E-13 | 4.79E-13 | 4.83E-13 |
| ReSe2@MIL-53@g-C3N4 | | 1.45E-08 | 1.46E-08 | 4.39E-12 | 4.42E-12 | 4.33E-12 | 4.33E-12 | 4.39E-12 |

Fig. 5 Anodic and cathodic peak currents *versus* scan rate for the (a) $ReSe_2$, (b) MIL-53(Fe)@$ReSe_2$, and (c) ReMIL-CN composite material and (d) oxidation and reduction diffusion coefficients of the three materials.

These anodic and cathodic peak current responses were analyzed to estimate the apparent ion transport kinetics, which revealed that the respective electrode facilitated fast and stable redox reactions during repeated cycling. Although the diffusion process could not be strictly described using classical solution-phase models, the relative changes in peak current intensities provided valuable insights into the electrochemical kinetics and ion diffusion efficiency. The obtained higher apparent anodic and cathodic responses corresponded to an intrinsic redox mechanism and suggested improved ionic mobility and facile electron transfer pathways, consistent with the synergistic effect of the ReMIL-CN framework and the conductive morphology. These findings indicated that the ReMIL-CN electrode exhibited a balanced combination of surface-controlled and diffusion-assisted charge storage, contributing to its superior electrochemical performance.

The highest obtained values of the diffusion coefficient "*D*" for both oxidation and reduction reactions were $D_{oxidation} = 4.87 \times 10^{-13}$ m$^2$ s$^{-1}$, $2.48 \times 10^{-12}$ m$^2$ s$^{-1}$, and $4.59 \times 10^{-8}$ m$^2$ s$^{-1}$ and $D_{reduction} = 5.67 \times 10^{-14}$ m$^2$ s$^{-1}$, $4.76 \times 10^{-13}$ m$^2$ s$^{-1}$, and $1.45 \times 10^{-8}$ m$^2$ s$^{-1}$ for the $ReSe_2$, MIL-53(Fe)@$ReSe_2$, and ReMIL-CN hybrid material, respectively. The highest obtained diffusion coefficient "*D*" for the ReMIL-CN compound confirmed the quicker kinetics of electroactive species towards this electrode. This rapid diffusion of charges to the electrode surface increased the resultant currents. A high value of *D* is also directly related to the sharpness of the redox peaks in CV plots, supporting surface suitability, a porous and rough surface nature, and a large effective surface area for redox reactions, leading to the tailoring of the reversibility of the electrode.

### 2.4 Electrochemical impedance spectroscopy (EIS)

The EIS analysis investigates the charge transfer dynamics of the prepared material-based electrode systems. The EIS results obtained for $ReSe_2$ and the ReMIL-CN composite material are presented in Fig. 6(a), which provides a detailed insight into the charge transfer resistive and capacitive interfacial properties of $ReSe_2$ and the ReMIL-CN hybrid composite material. In the high-frequency region of the Nyquist plot, a semicircle is observed, indicating the charge transfer resistance ($R_{ct}$) at the electrode/electrolyte interface. At high frequencies, the $ReSe_2$ exhibits a higher $R_{ct}$ value, as evident by its EIS arc with a larger semicircle, indicating the slower charge transfer kinetics of $ReSe_2$. In contrast, the ternary nanocomposite ReMIL-CN shows a smaller semicircle, reflecting a significantly reduced $R_{ct}$ and improved electrochemical performance resulting from the enhanced conductivity and synergistic interactions within the ReMIL-CN hybrid material. These results suggest improved

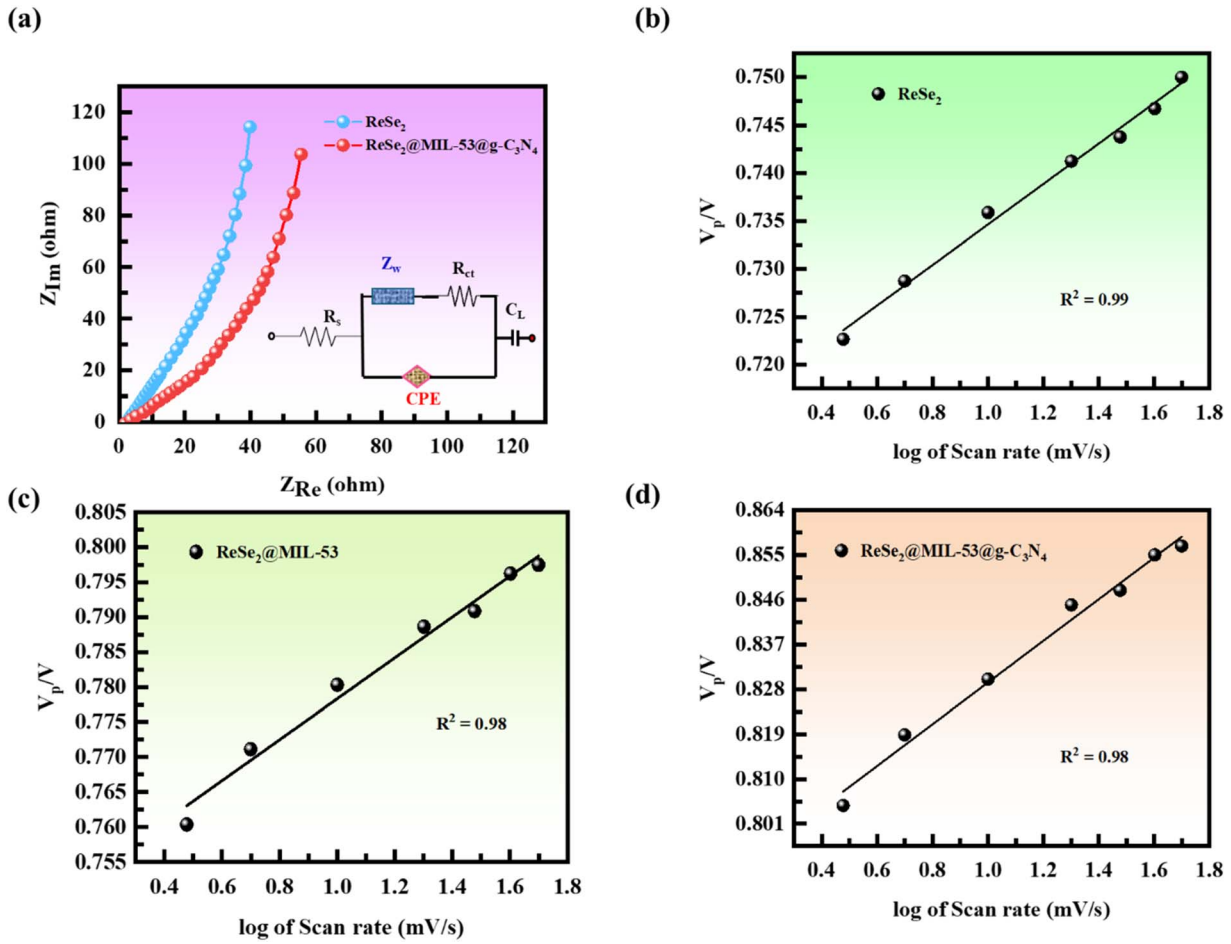


Fig. 6 (a) EIS measurement of $ReSe_2$ and MIL-53(Fe)@$ReSe_2$@g-$C_3N_4$ composite (b–d) peak voltage as a fuction of log of scan rate for $ReSe_2$, MIL-53(Fe)@$ReSe_2$, and ReMIL-CN composite.

electron transport and catalytic activity in the composite material, making it more favorable for efficient and fast energy storage applications. The EIS equivalent circuit model includes the series resistance ($R_s$) corresponding to the solution resistance. The semicircular region observed in the Nyquist plot corresponds to the charge transfer resistance ($R_{ct}$). The CPE demonstrates the constant phase element that accounts for the nonideal capacitive behavior at the electrode/electrolyte interface. Additionally, the Warburg impedance ($Z_w$) is associated with diffusion-controlled ion transport processes. The inclusion of these components assists in adjusting the overall electrochemical role of the ReMIL-CN nanocomposite's electrode and its ion diffusion, particularly at higher current densities.

To further elaborate on the charge storage mechanism, the correlational potential *versus* scan rate variation was studied, as shown in Fig. 6(b–d), for the three composites $ReSe_2$, MIL-53(Fe)@$ReSe_2$, and ReMIL-CN, corresponding to the peak currents in their respective CV analysis. The relative peak potential ($V_p/V$) of the output current *versus* scan rate variations for $ReSe_2$, MIL-53(Fe)@$ReSe_2$, and their ReMIL-CN nanocomposite electrodes, as shown in Fig. 6(d), reveals the strong linear relationships for the three electrodes, indicating the diffusion-controlled charge kinetics and stable electrochemical behavior of these electrodes. The pristine $ReSe_2$ electrode exhibits a correlation value of $R^2 = 0.99$, signifying an unhindered diffusion mechanism, while MIL-53(Fe)@$ReSe_2$ and the ReMIL-CN composite exhibit $R^2$ values of 0.98, suggesting similar diffusion-controlled processes. The variations in $R^2$ values for the hybrid composites can be attributed to structural and electronic enhancements due to the addition of Fe-MOF (MIL-53) and g-$C_3N_4$, which improve the performance, charge storage, and stability of these electrodes.

### 2.5 BET (nitrogen adsorption–desorption isotherm) analysis

The Brunauer–Emmett–Teller (BET) characteristic analysis was carried out *via* $N_2$-physisorption measurements using the Quantachrome Autosorb analyzing system. The obtained adsorption/desorption isotherms are presented in Fig. 7(a–d) for the $ReSe_2$, MIL-53(Fe), g-$C_3N_4$, and hybrid material electrodes, respectively. The material's porosity, including specific pore dimensions and their distribution, was measured from these isotherms.

All four samples exhibit type IV isotherms with noticeable hysteresis loops. These linearly rising hysteresis loops, observed within the relative pressure ($P/P_0$) range of 0.4–0.9, indicate capillary condensation within mesopores, confirming the mesostructured nature of the synthesized samples. The BET isotherm of $ReSe_2$, presented in Fig. 7(a), exhibits a type IV curve accompanied by a distinct H3-type hysteresis loop. This behavior is typical of mesoporous materials composed of nonrigid plate-like particle aggregates that form slit-shaped open pores due to the layered structure of $ReSe_2$.[60] The obtained BET hysteresis for MIL-53(Fe) suggests gradual monolayer-multilayer adsorption with an increase in the relative pressure. This hysteresis loop indicates that MIL-53 (Fe) possesses a mesoporous structure with flexible framework behavior, highlighting the material's dynamic adsorption properties.

The BET hysteresis for g-$C_3N_4$ demonstrates a less steep uptake curve and lower total nitrogen adsorption, implying the

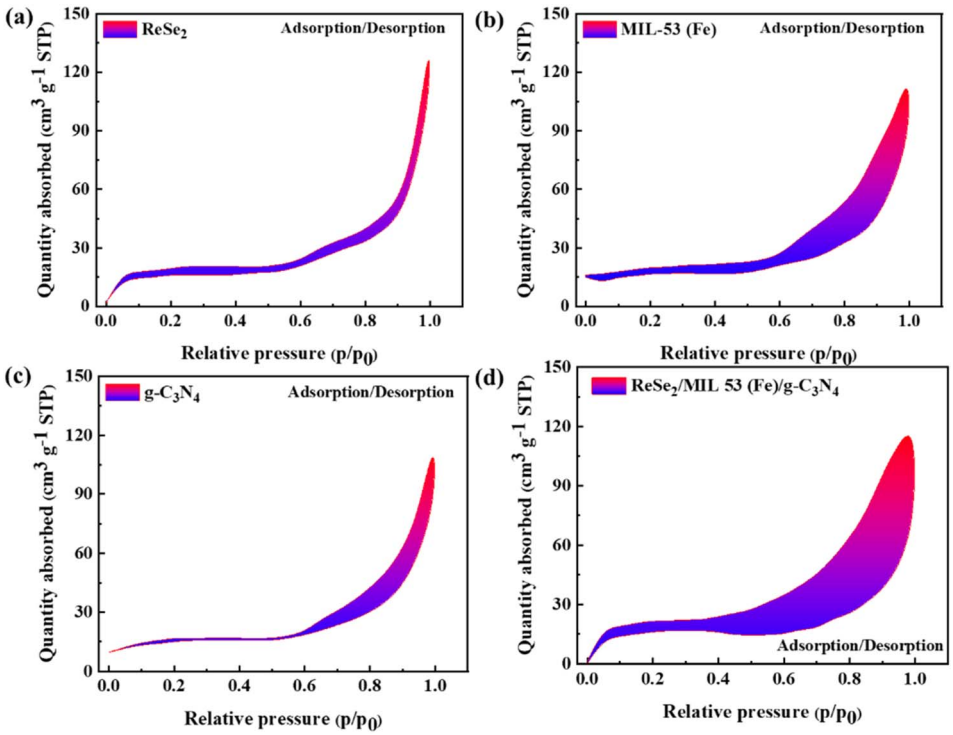


Fig. 7 BET analysis of the (a) $ReSe_2$, (b) MIL-53(Fe), (c) g-$C_3N_4$, and (d) ReMIL-CN composite electrodes.

relatively lower surface area and narrower pore distribution of this material. The BET results of the ReMIL-CN nanocomposite material, shown in Fig. 7(d), with a more pronounced hysteresis loop and a sharp increase in adsorption at higher relative pressures, demonstrate its highest $N_2$ uptake among all four materials. The observed trends reflect the superior adsorption performance of the ReMIL-CN hybrid composite, which is critical for specific applications in catalysis, gas storage, and separation. The total specific surface area and pore volume of the ReMIL-CN composite-based active electrode, estimated by the adsorbed/desorbed volume per gram ($cm^3\ g^{-1}$) of $N_2$ *versus* relative vapor pressure ($p/p_0$), are 154 $m^2\ g^{-1}$ and 0.022 $cm^3\ g^{-1}$, respectively. The significant surface area and pore size of this ReMIL-CN composite material reflect its readiness for efficient ion transport, storage, and release during high-energy and -power applications.

In the ReMIL-CN hybrid composite material, the layered structure of $ReSe_2$ facilitates the enhancement of ion intercalation and deintercalation across varying current densities by allowing ions to enter and exit the material easily during the charge–discharge process. The smooth and dispersed metallic linker Fe-MOF increases the overall surface area and available active sites of the electrode material, allowing it to store large quantities of ions and provide abundant pathways for ion diffusion. The Fe-MOF aids the device in maintaining a high capacity even at fast charging/discharging rates. The carbonaceous component (g-$C_3N_4$) introduces additional electronic pathways, leading to high electrical conductivity and fast ion transfer among the hybrid material's components. Overall, the electrochemical results affirm that the hierarchical structure of the ReMIL-CN composite's electrode offers substantial advantages for electrochemical energy storage applications by optimizing redox activity, structural stability, and electrical conductivity.

# 3 Real device applications

## 3.1 ReMIL-CN//AC hybrid device

The ReMIL-CN composite active electrode (AE) was further tested for real device ion storage applications in the standard two-electrode cell system with the second electrode of AC. The hybridization of the high specific energy and favorable cycling stability of the active electrode (AE) with the typically double-layered capacitive nature of the AC electrode leads to the benefits of both capacitive and faradaic processes in the hybrid system. The hybrid ReMIL-CN compound//AC electrode device is depicted in Fig. 8(a), with the WE being the active material ReMIL-CN. The two electrodes were immersed in a KOH electrolytic solution and were separated by a separator.

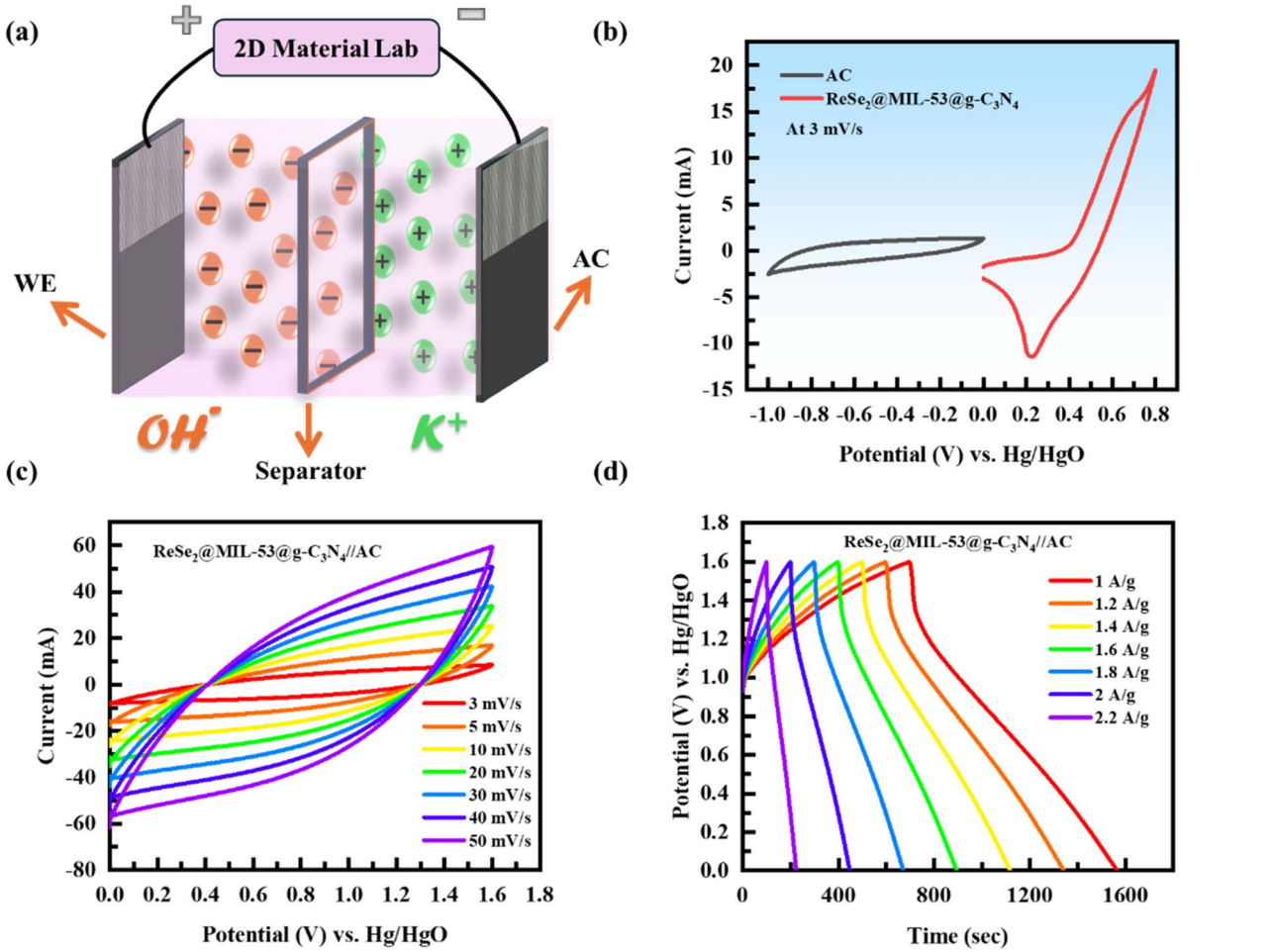


Fig. 8 (a) Real device depiction, (b) individual CV plots of the cathode and anode, and (c and d) hybrid device CV and GCD plots.

The CV results of ReMIL-CN composite and activated carbon (AC) electrodes are analysed using the three electrode systems as presented in Fig. 8(b). The results clearly indicates the capacitive response contribution of the AC electrode and faradaic response results presented by working electrode (WE). The counter electrode (AC) adds to the electrochemical capacitive performance by offering a highly stable and conductive surface area for substantial ion adsorption, thereby improving the overall energy density of the device. The CV and GCD plots in Fig. 8(c and d), respectively, provide a comprehensive understanding of the electrochemical behavior of the ReMIL-CN//AC hybrid device. The sharp and symmetric Faradaic redox peaks with quasi-rectangular-shaped CV curves and symmetric GCD profiles, even at higher scan rates, indicate rapid and reversible redox reactions dominated by surface-controlled charge storage rather than bulk ion diffusion. The excellent rate performance and minimal IR drop further confirm efficient electron/ion transport at the electrode–electrolyte interface.

Thus, the overall ReMIL-CN//AC device operates through a hybrid electrostatic–faradaic pseudocapacitive mechanism, ensuring high energy and power density with superior cycling stability. The area encapsulated by CV plots justifies its dominant charge storage mechanism and the storage capacity across the input voltages. These transitions highlight the significance of electrode design optimization, preparation methods, input potential ranges, and configurations, which can improve the electrochemical performance. The GCD analysis presented in Fig. 8(d) affirms the suitability of the ReMIL-CN composite//AC hybrid device for practical ion/energy storage applications. The consistent, symmetric, and stable GCD plots of the devised system show efficient electron flow with a minimal voltage drop and low internal resistance during the charging/discharging process. The influence of the counter electrode in the fabricated hybrid system is evidenced by the consistent, repeatable shape of the curves across cycles for a sustainable and stable capacity role over long-term cycling. This stability is crucial for practical applications, where the device needs to operate reliably during long-term charge–discharge cycles. The combination of the unique properties of each component material in the ReMIL-CN hybrid composite results in high ion storage and efficient ion delivery. Furthermore, the charge storage-specific capacity of the designed ReMIL-CN composite//AC cell system, evaluated from both CV and GCD plots, is about 423 C $g^{-1}$.

The cycling stability, columbic efficiency, and capacity retention of the ReMIL-CN composite//AC hybrid system were evaluated by subjecting it to 10 000 repeated electrochemical

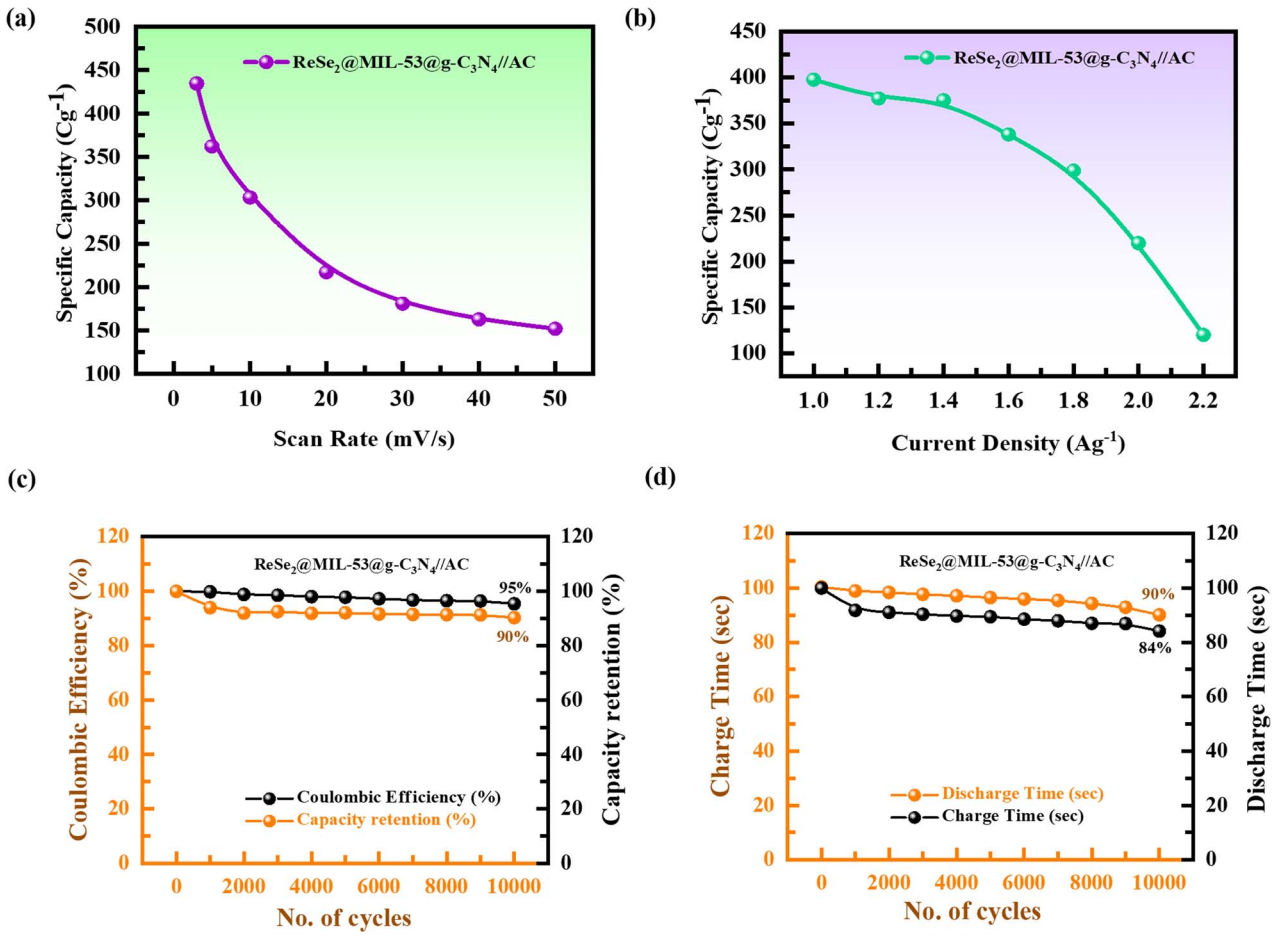


Fig. 9 (a and b) Specific capacity measurement results from CV, and GCD plots, (c and d) stability tests of the present hybrid device.

cycles under steady current conditions (Fig. 9). The presented fabricated device demonstrates an excellent 95% capacity retention, a 90% Columbic efficiency, and 90% and 84% charge–discharge cyclic retention stability, respectively. This suggests the structural and operational integrity of the ReMIL-CN composite//AC hybrid device over the prolonged operation of 10 000 cycles.

The *b*-value measurements of the devised system, as presented in Fig. 10(a), were employed to evaluate the charge storage behavior of the developed system. The *b*-values corresponding to the applied voltages of 0.6, 0.7, and 0.8 V were determined from the slope of the log–log plot of peak current ($\log i$) *versus* input scan rate ($\log v$). The slope $b = 0.59$ at 0.6 V suggests a predominantly diffusion-controlled process, which increases to $b = 0.68$ at 0.7 V, implying a transition towards a mixed contribution of surface-controlled capacitive and diffusion effects. Finally, at 0.8 V, the slope changes to $b = 0.7$, suggesting that surface-controlled processes become more prominent. The measured *b*-values indicate the hybrid charge storage behavior of the device, with diffusion-driven (battery-like) and surface-dominated capacitive characteristics. This behavior is desirable for tuning the hybrid (BHSC) response of the device. These observed *b*-values are indicative of the device's favorable ion kinetics, supporting rapid ion intercalation and deintercalation processes.

The study of the novel hybridized ReMIL-CN nanocomposite//AC system presented in this work highlights its outstanding rate capability at elevated voltages and current densities, along with high electrochemical storage response. The $E_d$ and $P_d$ values were measured from CV and GCD curves using the following eqn (5) and (6):

$$E_d = \frac{Q_s \times V}{2 \times 3.6} \quad (5)$$

$$P_d = \frac{E \times 3600}{\Delta t} \quad (6)$$

where $Q_s$ represents the specific capacity, $V$ is the operational voltage range, and $t$ is the discharge time.

The highest values of the specific energy ($E_d$) and specific power ($P_d$) obtained for the ReMIL-CN//AC-cell system are 50 Wh kg$^{-1}$ and 2060 W kg$^{-1}$, respectively. These values of $E_d$ and $P_d$ are comparable to or higher than those of many of the electrode materials documented in recent studies.

### 3.2 Dunn's model analysis

The charge storage behavior of the device was studied by separating the total current response into surface-controlled (capacitive) and diffusion-controlled contributions. Dunn's model plots in Fig. 11(a–c) present the relative contribution of these two storage mechanisms to the overall storage performance of the device with scan rate variations. At 3 mV s$^{-1}$, the diffusive contribution is close to 80%, while the capacitive contribution is around 20%, showing a strong contribution of the bulk (battery-type) behavior of the device. This is because at lower rates, the ions have more time to penetrate and accumulate within the electrode material. The capacitive contribution begins to increase with an increase in scan rates, and at 20 mV s$^{-1}$, the diffusive and capacitive parts reach nearly equal ratios. This reflects a balanced contribution of both mechanisms. At 50 mV s$^{-1}$, the capacitive contribution further increases, which corresponds to the dominance of surface redox processes, facilitating rapid ion transport and surface interactions at high input scan rates. The quantitative comparative analysis of surface-controlled and diffusion-controlled storage mechanisms, presented in Fig. 11(d), demonstrates a comprehensive analysis for the present system to achieve a balanced storage capacity. This Dunn's model analysis is valuable for adjusting our device's hybrid operational voltage range for fast ion intercalation and deintercalation applications that require high values of both energy and power densities.

The CV profiles of the as-configured $ReSe_2$//AC and $ReSe_2$@MIL-53//AC devices are shown in Fig. S1(a and d). These CV curves exhibit nearly rectangular shapes with slight redox humps, indicating a combination of electric double-layer capacitance and pseudocapacitive behavior. As the scan rate increases, the current response enhances proportionally

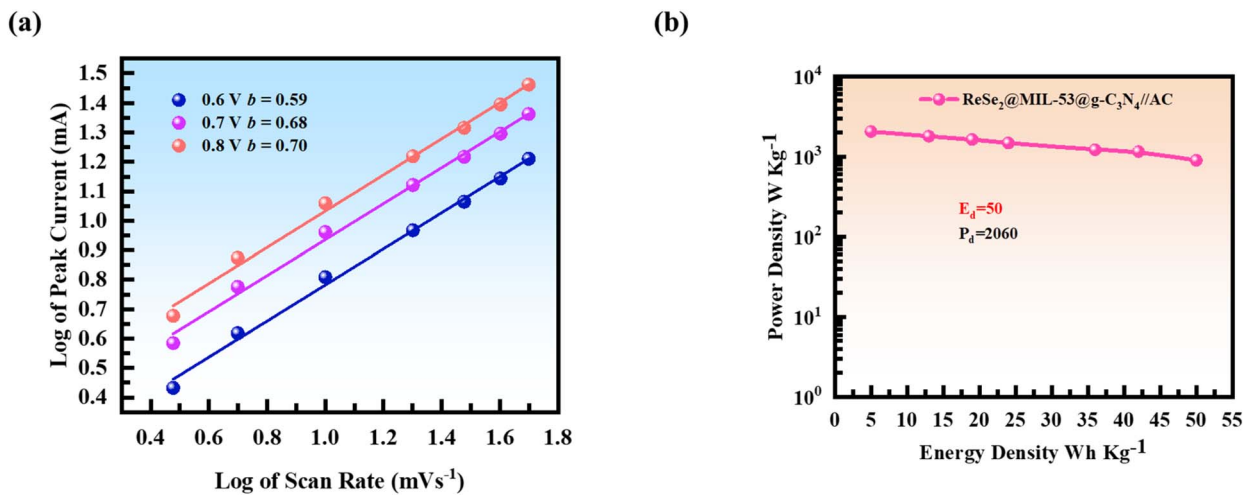


Fig. 10 (a) *b*-value measurement and (b) power density *versus* energy density Ragone plot.

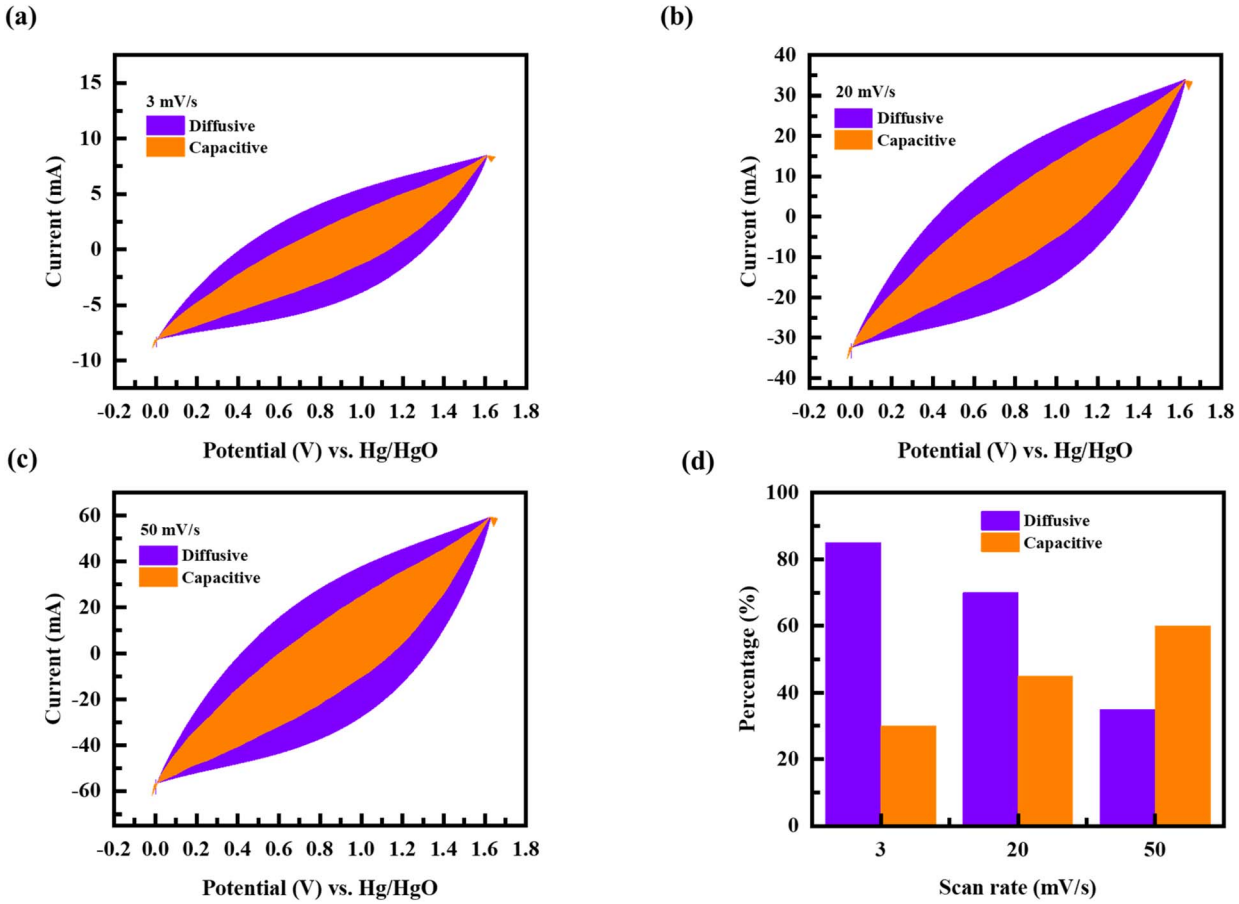


Fig. 11 (a–c) Results of Dunn's model and (d) comparison of the capacitive and diffusive response at 3, 20, and 50 mV $s^{-1}$.

without significant distortion, confirming excellent reversibility and rapid charge transfer capability. The stable shape of the CV profiles demonstrates good electrochemical stability and efficient ion diffusion within the electrode. According to the comparison plots of the three asymmetric-configured systems at a scan rate of 50 mV $s^{-1}$ in Fig. S2(a), the ReMIL-CN//AC device has a high area under the CV curve, indicating a higher charge storage capability and faster redox kinetics. This enhancement is attributed to the synergistic interaction between the transition metal selenide and the conductive g-$C_3N_4$ network, which facilitates efficient electron transfer and ion diffusion. Moreover, the nearly symmetrical redox peaks with a minimal potential shift at increasing scan rates reflect the excellent reversibility and rate capability of the composite. In contrast, the CV profiles of $ReSe_2$//AC and $ReSe_2$@MIL-53//AC cells show relatively smaller areas, implying slower reaction kinetics and a limited electroactive surface area. The GCD curves of $ReSe_2$//AC and $ReSe_2$@MIL-53//AC devices in Fig. S1(b and e) and GCD comparison plots of the three types of systems presented in Fig. S2(b) further corroborate the superior capacitive behavior of the hybrid electrode compared to its counterparts. All curves display nearly symmetric charge–discharge characteristics, indicating excellent reversibility and efficient charge-transfer kinetics. The discharge time decreases progressively with increasing current density, which can be attributed to limited ion diffusion at higher rates. The smooth potential–time curves further confirm good electrical conductivity and stable capacitive behavior. The comparison results demonstrate that the ReMIL-CN//AC device possesses high rate capability and reliable electrochemical performance suitable for energy storage applications,[61] with an extended discharge time, highlighting its enhanced energy storage capability. The excellent linearity and minimal IR drop observed in the GCD curves signify low internal resistance and high electrical conductivity. The improved electrochemical reversibility can be ascribed to the hierarchical architecture of the hybrid composite, where $C_3N_4$ sheets act as conductive bridges, preventing particle agglomeration and promoting rapid charge propagation throughout the electrode matrix. The specific capacity values calculated from the CV and GCD characteristic plots of $ReSe_2$// AC and $ReSe_2$@MIL-53//AC systems are presented in Fig. S1(c and f). The highest values of the specific capacities are 167.06 C $g^{-1}$ for the $ReSe_2$//AC system and 205.8 C $g^{-1}$ for $ReSe_2$@MIL-53//AC system. The $ReSe_2$@g-$C_3N_4$//AC electrode-based system outperforms, which delivers high capacity, with a gradual less decrease as the scan rate increases in comparison to $ReSe_2$// AC system. These measured values of the specific capacity are also lower than that of the hybrid electrode ReMIL–CN–based device (423 C $g^{-1}$). These findings confirm that the real ReMIL-CN//AC device outperforms the other developed composite

electrodes in terms of the specific capacity and electrochemical reversibility. The results collectively validate the effectiveness of our optimized ReMIL-CN composite-based system.

Based on the tunable efficiency and fast and high energy response of the present ReMIL-CN compound-based electrode, we have further evaluated its practical applicability in a hybrid device for the sensitive and selective detection of $H_2O_2$. It is a critical analyte in biomedical, food safety, and environmental monitoring applications, and its accurate and rapid detection is crucial, especially at trace levels.

### 3.3 Ternary ReMIL-CN composite-based electrode-integrated $H_2O_2$ detection system

For the $H_2O_2$ detection system configuration, the ReMIL-CN active electrode was tested based on its superior performance compared to other fabricated electrodes. The g-$C_3N_4$ provided a conducive platform for efficient electron transfer, the Fe-MOF introduced abundant active sites and porous channels to facilitate $H_2O_2$ diffusion and interaction, and $ReSe_2$ delivered high electrocatalytic activity for $H_2O_2$ oxidation.

Upon exposure to $H_2O_2$, the following electrocatalytic oxidation half-reaction occurred on the active electrode's surface:

$$H_2O_2 \rightarrow O_2 + 2H^+ + 2e^- \quad (7)$$

The generated electrons were transmitted efficiently to the electrode, resulting in a measurable current that was proportional to the concentration of $H_2O_2$. This current was recorded using a potentiostat, forming the basis of the quantitative detection of $H_2O_2$. We aimed to assess the stability, reproducibility, and selectivity of the ReMIL-CN hybrid composite-based electrode under simulated real-world conditions. For this, the hybrid device was exposed to varying concentrations of $H_2O_2$ in complex sample matrices. Differential pulse voltammetry (DPV) and chronoamperometry (CA) measurements were employed for electrochemical $H_2O_2$ sensing. From these results, the response time, LOD, linear range (with $R^2$ value), and sensitivity $\sigma$ of the sensor were quantified.

For electrochemical DPV analysis, a 0.1 M PBS electrolytic solution (with a pH value of 7.4) was used. The input scan rate potential was adjusted to 50 mV $s^{-1}$, corresponding to the effective output results, and the potential window was set from −0.2 V to +0.8 V *vs.* RHE (Hg/HgO). DPV curves were recorded at varying $H_2O_2$ concentrations ranging from 0 to 1000 μM (1 mM) with step values of 50, 100, 250, 500, 750, and 1000 μM. In the DPV plots presented in Fig. 12(a), clear anodic peaks were observed at 0.6 V *vs.* Hg/HgO, with peak currents increasing linearly as the $H_2O_2$ concentration increased. No noticeable redox peak was observed in the absence of $H_2O_2$ in the control test, as shown by the baseline current for 0 μM $H_2O_2$, clarifying the sensitivity and concentration-dependent response of the present modified electrode. Calibration curves obtained from the DPV plots shown in Fig. 12(b) demonstrated the linear dependence of peak current (*I*p) on the $H_2O_2$ concentration values, highlighting the suitability of the presented ReMIL-CN nanocomposite electrode for the $H_2O_2$ detection system. The sensitivity (*S*) of the device was measured from the slope of this calibration curve. The limit of detection (LOD) and limit of quantification (LOQ) were calculated using standard analytical equations, based on the standard deviation of the response and the slope of the calibration plot, as follows:

$$\mathrm{LOD} = \frac{3\sigma}{S} \quad (8)$$

$$\mathrm{LOQ} = \frac{10\sigma}{S} \quad (9)$$

Here, *S* is the sensitivity and $\sigma$ corresponds to the standard deviation of the blank signal.

The DPV curve corresponding to 0 μM served as a baseline measurement in the absence of the $H_2O_2$ analyte. The ReMIL-CN nanocomposite's modified electrode demonstrated an immediate current response time of 3 s for each $H_2O_2$ addition, corresponding to 95% of the final current values. This minor response time demonstrated the good reproducibility of the electrode in the real-time $H_2O_2$ detection system. The linear regression value of $R^2 = 0.989$ presented a high linear response of the electrode for $H_2O_2$ sensing, with a linear operating range (LOR) from 50 μM to 1000 μM. For concentrations above 1000 μM, the signal deviated from linearity, which may be due to sensor saturation and the diffusion limit of the electrode. The key performance metrics measured for the presented electrode were a sensitivity (*S*) of 0.185 μA $\mu M^{-1}$ $cm^{-2}$, an LOQ of 0.333 μM, and a LOD of 0.1 μM.

For the CA analysis, the applied potential was set at 0.6 V. The $H_2O_2$ concentration ranged from 0 to 1000 μM with a stepwise rise of 50, 100, 250, 500, and 750 μM every 50 seconds. This increase in the concentration values was followed by continuous stirring to maintain its uniform diffusion. The obtained current *vs.* time curve demonstrated consistent current plateaus after each addition of $H_2O_2$, indicating the modified electrode's rapid and highly stable response. The remarkable sensing capability of the electrode resulted from the synergistic interactions within the composite material. $ReSe_2$ provided high electrocatalytic activity for $H_2O_2$ decomposition, the Fe-MOF offered abundant active sites and porous channels for $H_2O_2$ diffusion, and g-$C_3N_4$ ensured efficient electron transport and structural integrity.[62] This combination enhanced sensitivity, fast response, and long-term stability, making the sensor suitable for real-time monitoring applications.

To elucidate the role of each component of the ReMIL-CN electrode in the $H_2O_2$ detection process, comparative electrochemical analyses were performed using $ReSe_2$, $ReSe_2$@MIL-53(Fe), and $ReSe_2$@MIL-53(Fe)@g-$C_3N_4$ electrodes. The DPV analysis plots of separate electrodes and comparative plots are shown in Fig. S3(a and c). The DPV peak potential and current intensity corresponded to the electrochemical reduction of $H_2O_2$ and varied notably depending on the structural composition, conductivity, and catalytic site distribution of each electrode material. Fig. S3(a) shows that the pristine $ReSe_2$ electrode exhibited a modest reduction current with a relatively positive peak potential, reflecting its moderate intrinsic conductivity and limited active site density. The layered

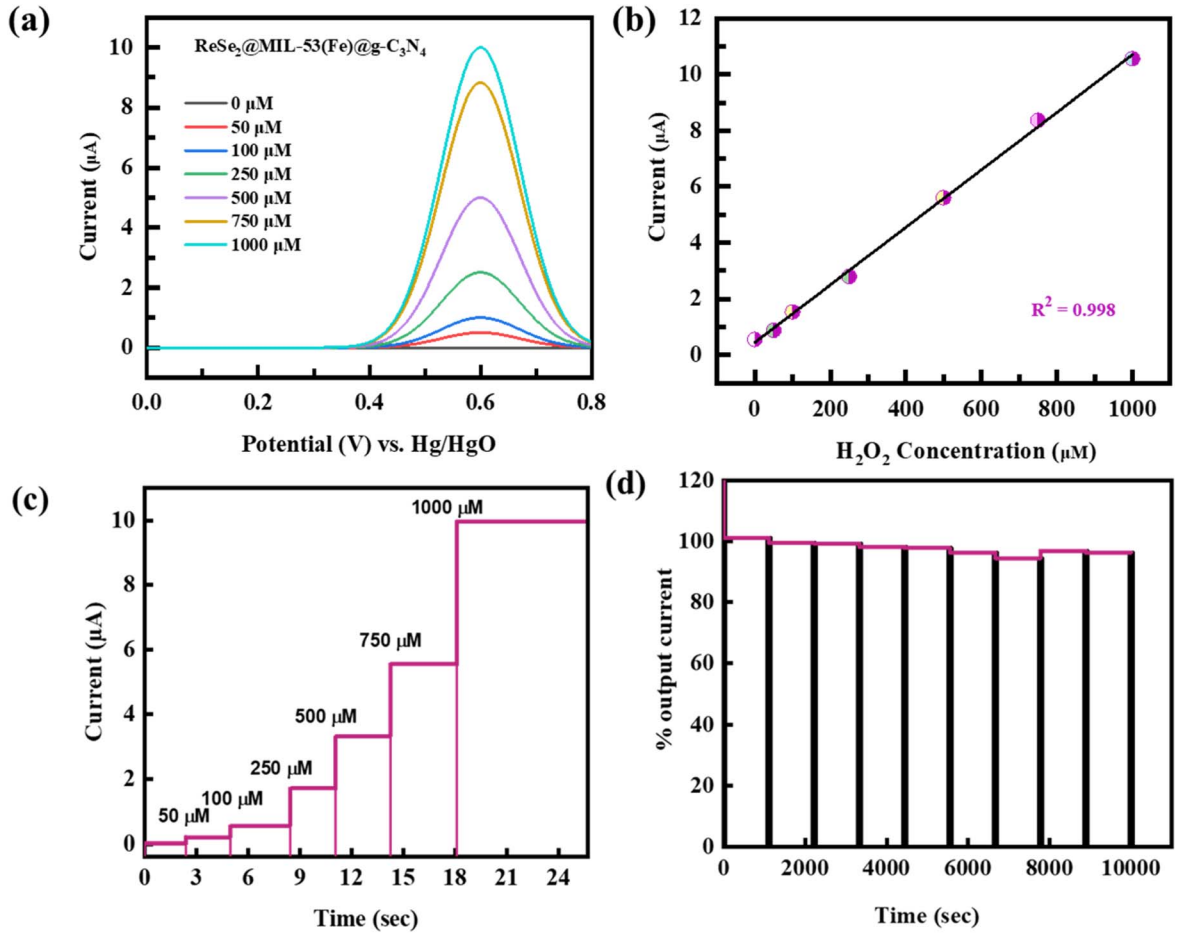


Fig. 12 (a) DPV curves at varying $H_2O_2$ concentrations, (b) calibration curve, (c) chronoamperometric (CA) evaluation of the response time, and (d) stability analysis for $H_2O_2$ sensing.

architecture and favorable Se-edge sites of $ReSe_2$ assisted charge transfer kinetics. The catalytic performance of the $ReSe_2$ electrode was somewhat hindered by the restricted number of reactive edges and weak adsorption affinity toward $H_2O_2$ molecules. The $ReSe_2$@MIL-53(Fe) electrode resulted in a noticeable enhancement in the catalytic current and a reduction in the onset potential. This is due to the Fe-based redox centers that promoted efficient electron mediation. The $ReSe_2$@MIL-53(Fe) electrode presented a distinctly enhanced DPV current response and a noticeable shift of the peak potential toward a more negative value. This enhancement facilitated the catalytic decomposition of $H_2O_2$ and served as an efficient electron mediator.[63] The porous MOF framework also increased the electrochemically active surface area and improved diffusion pathways for reactant molecules. The synergistic effect of the Fe nodes and the $ReSe_2$ conductive network promoted faster charge transfer and efficient utilization of active sites, as evidenced by the higher current density and reduced overpotential. The DPV plot comparison of $ReSe_2$, $ReSe_2$@MIL-53(Fe), and ReMIL-CN showed that the composite demonstrated the most pronounced catalytic behavior, characterized by the highest reduction peak current and the lowest overpotential. This improvement was primarily attributed to the introduction of the g-$C_3N_4$ nanosheets, which provided abundant nitrogen functionalities that acted as electron-donating centers and facilitated $H_2O_2$ adsorption through N–H and lone-pair interactions.[64] Overall, the g-$C_3N_4$ supplied nitrogen-rich anchoring sites and improved surface adsorption and electronic coupling. The calibration plots of three types of electrodes demonstrated the linear rise in output currents with increasing $H_2O_2$ concentration. The excellent linearity confirmed the reliable sensitivity and reproducibility of the hybrid electrode. The DPV comparison plots in Fig. S4 clearly demonstrate that the ReMIL-CN plays an amplified overall catalytic performance through interfacial charge coupling and structural stabilization, rendering the composite an excellent candidate for high-performance $H_2O_2$ sensing applications.

To substantiate the performance and reliability of the fabricated electrode and its applied studies, a comprehensive comparison was performed, shown in Fig. 13 in which we have benchmarked our results against a wide range of previously reported systems for both BHSC and $H_2O_2$ detection applications, establishing a clear context for evaluating the superior efficiency, sensitivity, and practicality of the present work.

Fig. 13(a) illustrates the comparative performance of key metrics, including retention stability, energy density ($E_d$), and

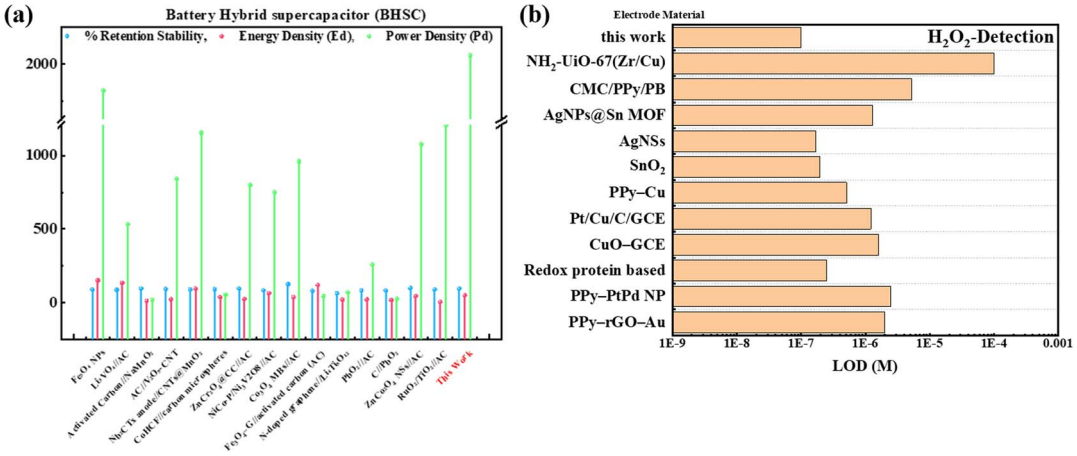


Fig. 13 Comparative analysis of the previously reported electrode materials for (a) BHSC-configured devices[65–76] and (b) LOD values for $H_2O_2$ detection systems.[77–87]

power density ($P_d$), of our ReMIL-CN//AC BHSC device against previously reported systems. This comparison demonstrates the notably superior overall performance of our benchmarked ReMIL-CN//AC device. It exhibits high energy and power densities of 50 Wh $kg^{-1}$ and 2060 W $kg^{-1}$, respectively, while maintaining commendable retention stability. Our presented ReMIL-CN//AC BHSC device presents the highest cohort $E_d$ value and significantly higher value for $P_d$, which indicates its potential for rapid energy delivery and efficient energy storage capability. The ReMIL-CN//AC system offers a balanced enhancement across all parameters. This demonstrates the efficacy of our material engineering strategy and highlights the practical applicability of our ReMIL-CN//AC-BHSC for advanced energy storage devices.

The LOD performance of the modified ReMIL-CN electrode was also evaluated and benchmarked against a range of previously reported materials for hydrogen peroxide ($H_2O_2$) detection, as illustrated in Fig. 13(b). Remarkably, the presented fabricated ReMIL-CN electrode-based sensor exhibits a significantly lower LOD, reaching the order of 0.1 μM, which is the lowest among all compared systems. This superior response indicates the exceptional ability of the fabricated electrode to detect trace levels of $H_2O_2$ with high precision. The enhanced performance of the presented ReMIL-CN electrode stems from its tailored nanostructure, increased electroactive surface area, and efficient electron transfer properties, which collectively facilitate the rapid and highly sensitive detection of $H_2O_2$. This positions the ReMIL–CN–based sensor as a highly competitive and promising candidate for advanced electrochemical biosensing applications, particularly where ultratrace level detection is essential.

## 4 Conclusion

This comprehensive study demonstrated the successful synthesis and characterization of a novel ReMIL-CN nanocomposite material comprising $ReSe_2$ (a 2D material), MIL-53(Fe) (an iron MOF), and g-$C_3N_4$. This study highlights the suitability of integrating this electrode into multifunctional electrochemical systems for energy storage and biochemical sensing applications. Structural, morphological, and electrochemical characterizations provided insights into its performance under varying loading conditions. The presented synthesized ReMIL-CN ($ReSe_2$@MIL-53(Fe)@g-$C_3N_4$) nanocomposite exhibited an average crystallite size of 27.27 nm, a BET-derived specific surface area of 154 $m^2\ g^{-1}$, and a BJH specific pore volume of 0.022 $cm^3\ g^{-1}$. The presented ReMIL-CN composite electrode exhibited remarkable performance, delivering specific capacities of 1925.5 C $g^{-1}$ in the three-electrode assembly setup and 423 C $g^{-1}$ in the two-electrode AC hybrid cell configuration. This hybrid device delivered high gravimetric energy and power densities of 50 Wh $kg^{-1}$ and 2060 W $kg^{-1}$, respectively. The ReMIL-CN composite//AC device demonstrated outstanding electrochemical cycling stability, with a 95% capacity retention, a 90% coulombic efficiency, and up to 90% and 84% charge–discharge time retention over the prolonged period of 10 000 cycles. The corresponding diffusion coefficients obtained for oxidation and reduction were $4.59 \times 10^{-8}\ m^2\ s^{-1}$ and $1.45 \times 10^{-8}\ m^2\ s^{-1}$, respectively. The measured *b*-values of 0.59, 0.68, and 0.70 confirmed the hybrid-natured operational mechanism of this device. BET analysis, Dunn's model evaluation, and EIS spectroscopy further illustrated the hybrid response of the presented device, highlighting the synergistic interaction among the $ReSe_2$, MIL-53(Fe), and g-$C_3N_4$ components of the presented composite-based electrode. Additionally, this ReMIL-CN composite-based modified electrode demonstrated the high sensitivity value of 0.185 μA $\mu M^{-1}\ cm^{-2}$, with an LOR of 50-1000 μM, and an efficient LOD of 0.1 μM in $H_2O_2$ sensing applications. The sensing platform retained 95% signal stability after 1000 cycles with a linearity of $R^2 = 0.998$ and a rapid response time of less than 3 seconds, indicating the good selectivity and repeatability of the system. The acquired long-term operational stability, rapid response time, minimal signal deviation, and stable reusability response confirmed the reliability and adaptability of the presented ternary composite ReMIL-CN electrode for $H_2O_2$ sensing,

making it usable in practical applications beyond the controlled laboratory settings, to evaluate matrix effects on sensor response in biological fluids and food extracts.

The presented comprehensive investigations highlighted the potential of the presented hybrid composite as a versatile multifunctional electrode material for dual-purpose electrochemical energy storage and hydrogen peroxide detection systems. Its dual functioning capability suggests a unique multifunctional advantage, where the electrode not only contributes to advanced energy storage but also enables real-time biochemical sensing. This feature positions it as a strong candidate for next-generation smart, self-powered bioelectrochemical devices and integrated health-monitoring supercapacitors, where energy storage and molecular detection functionalities coexist. It also paves the way for portable and wearable diagnostic technologies, food quality control, and environmental analysis. This synergistic approach not only enhances the practical utility of the electrode but also aligns with current trends in miniaturized, multifunctional, and wearable electronic devices.

## Conflicts of interest

There are no conflicts of interest to declare.

## Data availability

The data are available on request.

Supplementary information: Fig. S1 and S2: device level performance and comparison of $ReSe_2$//AC and $ReSe_2$@MIL-53//AC; Fig. S3 and S4: DPV curves, comparison and calibration plots of $ReSe_2$ and $ReSe_2$@MIL-53 composite. See DOI: **https://doi.org/10.1039/d5ra06541k**.

## Acknowledgements

The authors express their gratitude to the support of Princess Nourah bint Abdulrahman University Researchers Supporting Project number (PNURSP2025R58), Princess Nourah bint Abdulrahman University, Riyadh, Saudi Arabia. The authors also extend special thanks to Yeungnam University (Republic of Korea) for providing facilities to realize this work.

## References

1 M. Amir, *et al.*, Energy storage technologies: An integrated survey of developments, global economical/environmental effects, optimal scheduling model, and sustainable adaption policies, *J. Energy Storage*, 2023, **72**, 108694.
2 M. K. Khawaja, A. Alkhalidi and S. Mansour, Environmental impacts of energy storage waste and regional legislation to curtail their effects–highlighting the status in Jordan, *J. Energy Storage*, 2019, **26**, 100919.
3 I. Hadjipaschalis, A. Poullikkas and V. Efthimiou, Overview of current and future energy storage technologies for electric power applications, *Renew. Sustain. Energy Rev.*, 2009, **13**(6–7), 1513–1522.
4 S. P. Badwal, *et al.*, Emerging electrochemical energy conversion and storage technologies, *Front. Chem.*, 2014, **2**, 79.
5 I. T. Bello, *et al.*, Electrochemical Energy Conversion and Storage Systems: A Perspective on the Challenges and Opportunities for Sustainable Energy in Africa, *Energy Rev.*, 2024, 100109.
6 I. Kamaraj and S. Kamaraj, Introduction to Energy Storage and Conversion, in Materials for Boosting Energy Storage, *Advances in Sustainable Energy Technologies*, ACS Publications, 2024, p. 1–27.
7 A. K. Worku, *et al.*, Energy storage technologies; recent advances, challenges, and prospectives, in *Planning of Hybrid Renewable Energy Systems, Electric Vehicles and Microgrid: Modeling, Control and Optimization*, Springer, 2022, p. 125–150.
8 A. Aghmadi and O. A. Mohammed, Energy Storage Systems: Technologies and High-Power Applications, *Batteries*, 2024, **10**(4), 141.
9 J. M. Tarascon, Towards sustainable and renewable systems for electrochemical energy storage, *ChemSusChem: Chemistry & Sustainability Energy & Materials*, 2008, **1**(8-9), 777–779.
10 J. O. Besenhard and M. Winter, Insertion reactions in advanced electrochemical energy storage, *Pure Appl. Chem.*, 1998, **70**(3), 603–608.
11 P. Poizot and F. Dolhem, Clean energy new deal for a sustainable world: from non-CO 2 generating energy sources to greener electrochemical storage devices, *Energy Environ. Sci.*, 2011, **4**(6), 2003–2019.
12 B. Lin, *et al.*, Enhanced peroxymonosulfate activation by Co/Mn and P modified carbon nitride for ciprofloxacin degradation: Performance, mechanism and toxicity assessment, *J. Environ. Chem. Eng.*, 2025, **13**(3), 116604.
13 P. Barman, *et al.*, Renewable energy integration with electric vehicle technology: A review of the existing smart charging approaches, *Renew. Sustain. Energy Rev.*, 2023, **183**, 113518.
14 G. Navarro, *et al.*, Present and future of supercapacitor technology applied to powertrains, renewable generation and grid connection applications, *Energies*, 2021, **14**(11), 3060.
15 S. Koohi-Kamali, *et al.*, Emergence of energy storage technologies as the solution for reliable operation of smart power systems: A review, *Renew. Sustain. Energy Rev.*, 2013, **25**, 135–165.
16 M. Hannan, *et al.*, Hydrogen energy storage integrated battery and supercapacitor based hybrid power system: A statistical analysis towards future research directions, *Int. J. Hydrogen Energy*, 2022, **47**(93), 39523–39548.
17 M. Pathak, *et al.*, High energy density supercapacitors: an overview of efficient electrode materials, electrolytes, design, and fabrication, *Chem. Rec.*, 2024, **24**(1), e202300236.
18 S. Nayak, D. Joshi and S. Nayak, Leveraging supercapacitors to mitigate limitations and enhance the performance of battery energy storage systems: A simulation and experimental validation, *Discover Energy*, 2024, **4**(1), 18.
19 M. Czagany, *et al.*, Supercapacitors: An efficient way for energy storage application, *Materials*, 2024, **17**(3), 702.

20 M. Z. Iqbal and U. Aziz, Supercapattery: Merging of battery-supercapacitor electrodes for hybrid energy storage devices, *J. Energy Storage*, 2022, **46**, 103823.
21 M. Pershaanaa, *et al.*, Every bite of Supercap: A brief review on construction and enhancement of supercapacitor, *J. Energy Storage*, 2022, **50**, 104599.
22 Y. Bajaj, *et al.*, Low Viscosity Ionic Liquids as Novel Dopants in Poly (Methyl Methacrylate) Polymer Electrolyte: Detailed Photoelectrochemical Studies, *Recent Innovations Chem. Eng.*, 2024, **17**(1), 3–25.
23 S. V. Sadavar, S. Y. Lee and S. J. Park, Advancements in asymmetric supercapacitors: From historical milestones to challenges and future directions, *Adv. Sci.*, 2024, 2403172.
24 S. Mumtaz, *et al.*, Synergistic integration of 3D-$ZnTb_2O_4$@1D-CNT@2D-rGO: A multi-dimensional hybrid electrode on carbon paper for highly-efficient energy and HER catalysis applications, *Diamond Relat. Mater.*, 2025, **159**, 112784.
25 P. Geng, *et al.*, Transition metal sulfides based on graphene for electrochemical energy storage, *Adv. Energy Mater.*, 2018, **8**(15), 1703259.
26 M. Jalalah, Green synthesis of Bi-metallic MXene (Mo2TiC2Tx)@ NiCo-MOF@ AC nanocomposite electrode for high-performance electrochemical energy storage, HER, ORR and photochemical applications, *Ceram. Int.*, 2025, **51**(21), 47417–47431.
27 M. Asif, *et al.*, Unveiling microbiologically influenced corrosion engineering to transfigure damages into benefits: a textile sensor for H2O2 detection in clinical cancer tissues, *Chem. Eng. J.*, 2022, **427**, 131398.
28 J. V. Kumar, *et al.*, Fabrication of potato-like silver molybdate microstructures for photocatalytic degradation of chronic toxicity ciprofloxacin and highly selective electrochemical detection of H2O2, *Sci. Rep.*, 2016, **6**(1), 34149.
29 N. Muhammad, *et al.*, Ion chromatography: A comprehensive review of sample preparation methods for analysis of halogens and allied nonmetals in critically challenging inorganic matrices, *J. Chromatogr. A*, 2024, 465311.
30 W. Wu, *et al.*, Facile and rapid room-temperature electrosynthesis and controlled surface growth of Fe-MIL-101 and Fe-MIL-101-NH2, *ACS Cent. Sci.*, 2021, **7**(8), 1427–1433.
31 X. Huang, B. Jiang, and Y. Liu, A reconfigurable battery supercapacitor hybrid energy system with active balancing for vehicle applications, in *2021 IEEE 19th International Power Electronics and Motion Control Conference (PEMC)*, IEEE, 2021.
32 Y. Zheng, Sulfur-doped g-$C_3N_4$/rGO porous nanosheets for highly efficient photocatalytic degradation of refractory contaminants, *J. Mater. Sci. Technol.*, 2020, **41**, 117–126.
33 N. Kumar, *et al.*, Recent advancements in zero-to three-dimensional carbon networks with a two-dimensional electrode material for high-performance supercapacitors, *Nanoscale Adv.*, 2023, **5**(12), 3146–3176.
34 Z. Cai, *et al.*, Dynamic Study of Intercalation/Deintercalation of Ionic Liquids in Multilayer Graphene Using an Alternating Current Raman Spectroscopy Technique, *J. Phys. Chem. Lett.*, 2023, **14**(32), 7223–7228.
35 M. Sadiq, *et al.*, MXene-montmorillonite nanocomposites-based scaffold sensors for early pancreatic cancer diagnosis, *Cancer Plus*, 2024, **6**(3), 3793.
36 J. Li, *et al.*, Ultrasensitive electrochemical sensor for fenitrothion based on MIL-125 derived iron/titanium bimetallic oxides doped porous carbon composite, *Microchem. J.*, 2024, **200**, 110426.
37 Z. Zhao, *et al.*, From Body Monitoring to Biomolecular Sensing: Current Progress and Future Perspectives of Triboelectric Nanogenerators in Point-of-Care Diagnostics, *Sensors*, 2024, **24**(2), 511.
38 K. Subhani, *et al.*, Multifunctional structural composite supercapacitors based on MnO2-nanowhiskers decorated carbon fibers, *J. Energy Storage*, 2022, **56**, 105936.
39 C. Xia, *et al.*, Spotlighting the boosted energy storage capacity of CoFe2O4/Graphene nanoribbons: a promising positive electrode material for high-energy-density asymmetric supercapacitor, *Energy*, 2023, **270**, 126914.
40 J. Hao, *et al.*, Designing a hybrid electrode toward high energy density with a staged Li+ and PF6− deintercalation/intercalation mechanism, *Proc. Natl. Acad. Sci. U. S. A.*, 2020, **117**(6), 2815–2823.
41 P. Hu, *et al.*, NaV3 (PO4) 3/C nanocomposite as novel anode material for Na-ion batteries with high stability, *Nano Energy*, 2016, **26**, 382–391.
42 P. Sakthivel, *et al.*, Electrochemical energy storage applications of carbon nanotube supported heterogeneous metal sulfide electrodes, *Ceram. Int.*, 2022, **48**(5), 6157–6165.
43 X. Cui, *et al.*, Intercalation chemistry engineering strategy enabled high mass loading and ultrastable electrodes for High-Performance aqueous electrochemical energy storage devices, *J. Colloid Interface Sci.*, 2024, **660**, 32–41.
44 R. Sahoo, *et al.*, Fast-charging high-energy battery–supercapacitor hybrid: anodic reduced graphene oxide–Vanadium (IV) Oxide Sheet-on-Sheet Heterostructure, *ACS Nano*, 2019, **13**(9), 10776–10786.
45 F. Alam, *et al.*, Binary composites of sonochemically synthesized cobalt phosphates/polyaniline for supercapattery devices, *J. Energy Storage*, 2021, **42**, 103150.
46 V. P. Nguyen, *et al.*, Intercalation-Conversion Hybrid Cathode Enabled by MXene-Driven TiO2/TiS2 Heterostructure for High-Energy-Density Li–S Battery, *Small Struct.*, 2024, **5**(8), 2400196.
47 A. Ahmad, *et al.*, Improved Electrochemical Performance of Aqueous Hybrid Supercapacitors Using CrCo2O4 Mesoporous Nanowires: An Innovative Strategy toward Sustainable Energy Devices, *ACS Appl. Mater. Interfaces*, 2024, **16**(6), 6920–6930.
48 J. He, *et al.*, Intercalation-type catalyst for non-aqueous room temperature sodium-sulfur batteries, *Nat. Commun.*, 2023, **14**(1), 6568.
49 F. Zhang, *et al.*, A high-performance supercapacitor-battery hybrid energy storage device based on graphene-enhanced electrode materials with ultrahigh energy density, *Energy Environ. Sci.*, 2013, **6**(5), 1623–1632.

50 Y. Zhang, J. Lao and P. Xiao, Anion Intercalation/De-Intercalation Mechanism Enabling High Energy and Power Densities of Lithium-Ion Capacitors, *Batteries*, 2024, **10**(9), 296.
51 N. Naresh, *et al.*, Integrated Structural Modulation Inducing Fast Charge Transfer in Aqueous Zinc-Ion Batteries, *Small*, 2024, 2406249.
52 B. Polat, *et al.*, ZnO@ Polypyrrole-P (VSANa) on flexible and wearable carbon felt as electrodes for nonenzymatic H2O2 sensor and supercapacitor applications, *J. Mater. Res.*, 2024, **39**(6), 913–927.
53 J. Zhao, *et al.*, Optimizing electronic structure of Mo2TiC2Tx MXene through Nb doping for enhanced electrochemical performance, *Nano Res.*, 2024, 1–8.
54 C. Xiong, *et al.*, Fabrication of eco-friendly carbon microtubes@ nitrogen-doped reduced graphene oxide hybrid as an excellent carbonaceous scaffold to load MnO2 nanowall (PANI nanorod) as bifunctional material for high-performance supercapacitor and oxygen reduction reaction catalyst, *J. Power Sources*, 2020, **447**, 227387.
55 A. Mohammad and M. A. Zamzami, Construction of carbon cloth modified-Al2O3-g-C3N4 sensor for non-enzymatic electrochemical detection of hydrogen peroxide, *Diamond Relat. Mater.*, 2023, **132**, 109600.
56 H. Xu, *et al.*, Alternating Multilayered $Ti_3C_2T_x$/Co Sandwich with Co Frosting for Superior Electromagnetic Wave Absorption Performance and Infrared Stealth Ability, *ACS Appl. Mater. Interfaces.*, 2025, **17**(33), 47679–47695.
57 H. Azizi-Toupkanloo, *et al.*, Photocatalytic mineralization of hard-degradable morphine by visible light-driven Ag@ gC 3 N 4 nanostructures, *Environ. Sci. Pollut. Res.*, 2019, **26**, 30941–30953.
58 A. Ghetiya, *et al.*, Growth, characterizations, and thermal analysis of rhenium chalcogenides ReS2− x Se x (x= 0, 1, and 2) single crystals, *J. Mater. Sci.: Mater. Electron.*, 2023, **34**(2), 122.
59 G. Lacarbonara, *et al.*, A MnO x–graphitic carbon composite from CO 2 for sustainable Li-ion battery anodes, *Mater. Adv.*, 2022, **3**(18), 7087–7097.
60 K. Sato, E. Fujikawa and J. A. Cecilia, Increased protonation of a mesopore surface in a porous clay nanoheterostructure, *J. Phys. Chem. C*, 2022, **126**(30), 12615–12622.
61 R. Mysyk, *et al.*, The Value Chain of Sustainable Dual Carbon Sodium Ion Capacitors, *Batteries Supercaps*, 2025, e202400807.
62 J. Muthu, *et al.*, Review of extrinsic factors that limit the catalytic performance of transition metal dichalcogenides (TMDs) in hydrogen evolution reactions (HER), *ChemElectroChem*, 2024, **11**(17), e202400259.
63 C.-W. Bai, *et al.*, Circumventing bottlenecks in H2O2 photosynthesis over carbon nitride with iodine redox chemistry and electric field effects, *Nat. Commun.*, 2024, **15**(1), 4718.
64 A. A. Almunyif, *et al.*, Synergistic $Ni(OH)_2$@$Li_4Ti_5O_{12}$@ B/N-doped graphene architecture: Pioneering high-energy hybrid supercapacitors with superior electrocatalytic performance, *Inorg. Chem. Commun.*, 2025, **181**(2), 115243.
65 T. Govindasamy, *et al.*, Modulating the structural and magnetic properties of Fe3O4 NPs for high-performance supercapattery and EMI shielding applications, *J. Energy Storage*, 2024, **79**, 110243.
66 L. Shen, *et al.*, Peapod-like Li3VO4/N-doped carbon nanowires with pseudocapacitive properties as advanced materials for high-energy lithium-ion capacitors, *Adv. Mater.*, 2017, **29**(27), 1700142.
67 D. Cericola and R. Kötz, Hybridization of rechargeable batteries and electrochemical capacitors: Principles and limits, *Electrochim. Acta*, 2012, **72**, 1–17.
68 R. S. Ingole, *et al.*, One-Pot Hydrothermal Synthesis of Vanadium Oxide-Decorated Carbon Nanotube Hybrid Composite Electrodes for Superior Supercapacitor Applications, *Adv. Mater. Technol.*, 2025, e00045.
69 Z. Zou, *et al.*, Excellent Zinc-Ion Hybrid Capacitor Based on the Nb2CT x Anode and CNTs@ MnO2 Nanocomposite Cathode, *ACS Appl. Nano Mater.*, 2024, **7**(17), 20645–20652.
70 K. Lu, *et al.*, High-energy cobalt hexacyanoferrate and carbon micro-spheres aqueous sodium-ion capacitors, *J. Power Sources*, 2016, **303**, 347–353.
71 S. Suganya, *et al.*, Investigations of ternary Cu-Mn-Zn oxide nanocomposites as potential electrode for hybrid supercapacitors by one-pot hydrothermal method, *J. Energy Storage*, 2025, **109**, 115181.
72 Y. Hao, *et al.*, Highly dispersive nickel vanadium oxide nanoparticles anchored on nickel cobalt phosphate micron-sheets as cathodes for high-energy hybrid supercapacitor devices, *J. Alloys Compd.*, 2025, **1010**, 177893.
73 H. Chen, *et al.*, Template-free synthesis of novel Co3O4 micro-bundles assembled with flakes for high-performance hybrid supercapacitors, *Ceram. Int.*, 2021, **47**(1), 716–724.
74 S. Zhang, *et al.*, High Performance Lithium-Ion Hybrid Capacitors Employing Fe3O4–Graphene Composite Anode and Activated Carbon Cathode, *ACS Appl. Mater. Interfaces*, 2017, **9**(20), 17136–17144.
75 N. Yu, *et al.*, Electrodeposited PbO2 thin film as positive electrode in PbO2/AC hybrid capacitor, *Electrochim. Acta*, 2009, **54**(14), 3835–3841.
76 H. Sun, *et al.*, Battery-type ZnCo2O4 nanosheets and nanowires as advanced cathode materials for hybrid supercapacitors with ultra-long cycling stability, *J. Energy Storage*, 2024, **92**, 112189.
77 D. Mathivanan, *et al.*, Novel polypyrrole-graphene oxide-gold nanocomposite for high performance hydrogen peroxide sensing application, *Sensor Actuator Phys.*, 2021, **328**, 112769.
78 M. Lin, *et al.*, Hydrogen peroxide detection using a polypyrrole/Prussian blue nanowire modified electrode, *Macromol. Res.*, 2011, **19**, 673–678.
79 B. K. Jena and C. R. Raj, Enzyme integrated silicate–Pt nanoparticle architecture: A versatile biosensing platform, *Biosens. Bioelectron.*, 2011, **26**(6), 2960–2966.
80 L. Zhang, *et al.*, Facile synthesis of flower like copper oxide and their application to hydrogen peroxide and nitrite sensing, *Chem. Cent. J.*, 2011, **5**, 1–9.

81 M. Janyasupab, *et al.*, Bimetallic Pt–M (M= Cu, Ni, Pd, and Rh) nanoporous for H2O2 based amperometric biosensors, *Sens. Actuators, B*, 2013, **179**, 209–214.
82 P. M. Nia, W. P. Meng and Y. Alias, One-step electrodeposition of polypyrrole-copper nano particles for H2O2 detection, *J. Electrochem. Soc.*, 2015, **163**(3), B8.
83 S. Beenaben, R. Sankararajan and M. Kumaresan, Investigation on electrochemical sensing behavior of hydrogen peroxide using tin dioxide (SnO2) nanoparticles, *J. Mater. Sci.: Mater. Electron.*, 2025, **36**(12), 705.
84 B. Ma, *et al.*, A sensitive electrochemical nonenzymatic biosensor for the detection of H2O2 released from living cells based on ultrathin concave Ag nanosheets, *Biosens. Bioelectron.*, 2018, **106**, 29–36.
85 M. Z. Abedeen, L. Yadav and R. Gupta, Sensitive electrochemical determination of hydrogen peroxide in milk and water utilizing AgNPs@ Sn MOF nanozyme, *Microchim. Acta*, 2025, **192**(3), 152.
86 S. Uzunçar, N. Özdoğan and M. Ak, Amperometric detection of glucose and H2O2 using peroxide selective electrode based on carboxymethylcellulose/polypyrrole and Prussian Blue nanocomposite, *Mater. Today Commun.*, 2021, **26**, 101839.
87 P.-h. Ling, *et al.*, A metal–organic framework with multienzyme activity as a biosensing platform for real-time electrochemical detection of nitric oxide and hydrogen peroxide, *Analyst*, 2021, **146**(8), 2609–2616.